

Chiral metals and entrapped insulators in a one-dimensional topological non-Hermitian system

Ayan Banerjee,^{1,*} Suraj S. Hegde^{2,3,†} Adhip Agarwala,^{3,4,‡} and Awadhesh Narayan^{1,§}

¹*Solid State and Structural Chemistry Unit, Indian Institute of Science, Bangalore 560012, India*

²*Institut für Theoretische Physik, Technische Universität Dresden, 01069 Dresden, Germany*

³*Max-Planck Institute for the Physics of Complex Systems, Nöthnitzer Straße 38, Dresden 01187, Germany*

⁴*International Centre for Theoretical Sciences, Tata Institute of Fundamental Research, Bengaluru 560089, India*



(Received 23 November 2021; revised 9 March 2022; accepted 4 April 2022; published 2 May 2022)

In this work, we study many-body “steady states” that arise in the non-Hermitian generalization of the noninteracting Su-Schrieffer-Heeger model at a finite density of fermions. We find that the hitherto known phase diagrams for this system, derived from the single-particle gap closings, in fact correspond to distinct nonequilibrium phases, which either carry finite currents or are dynamical insulators where particles are entrapped. Each of these have distinct quasiparticle excitations and steady-state correlations and entanglement properties. Looking at finite-sized systems, we further modulate the boundary to uncover the topological features in such steady states, particularly the emergence of leaky boundary modes. Using a variety of analytical and numerical methods, we develop a theoretical understanding of the various phases and their transitions, and we uncover the rich interplay of nonequilibrium many-body physics, quantum entanglement, and topology in a simple looking yet rich model system.

DOI: [10.1103/PhysRevB.105.205403](https://doi.org/10.1103/PhysRevB.105.205403)

I. INTRODUCTION

Quantum matter and its novel manifestations are often characterized by an intricate interplay of quantum fluctuations, ideas of band topology, and entanglement [1–5]. A rather new addition to this group has been the notion of non-Hermiticity, which has its own illustrious history of being visited time and again, in the context of dynamical systems, open systems, or parity-time (PT) symmetric systems, which have been realized in various physical platforms [6–22]. While one strategy has been to investigate the role of non-Hermiticity that arises in the effective Hamiltonian of some degrees of freedom (due to coupling to a bath or leads, etc.), another has been to sideline the above question and explicitly model the non-Hermitian Hamiltonians and investigate their properties.

A plethora of work, in recent years, has been dedicated to this latter theme, and, in particular, the role of non-Hermiticity in lattice models has been widely investigated [6–9,20]. Most notable among this class of works has been the investigations into the role of topology *vis-à-vis* non-Hermiticity. While building a catalog of such results would be an impossible task here, we point out the underlying themes that have been in discussion in the literature (see Refs. [6–9,20] for recent reviews). The introduction of non-Hermiticity, in general, in the Hamiltonian matrix results in complex eigenvalues, which leads to the idea of a band diagram being generalized to a

complex energy plane, where the notion of a band gap is modified to the prohibition of touching a base energy in the complex spectrum [23]. Thus a new notion of “a topological phase” was introduced in these systems, which involves winding of the single-particle energies over the entire complex spectra [23–25]. It is important to note, however, that such a winding is inherently distinct from the case in which a half-filled Hermitian system is called “topological,” where it is often a response of the many-particle state in equilibrium that can be written in terms of such topological quantities that quantify the behavior of single-particle wave functions over the Brillouin zone [26–28]. The absence of this latter connection is a result of a rather incomplete understanding between the many-body state of a non-Hermitian noninteracting system and its single-particle complex eigenspectrum, as we discuss below.

While the object of interest in Hermitian lattice tight-binding models is the ground state and its low-energy excitations, in a non-Hermitian system the appearance of complex eigen-spectra requires us to restructure the framework for characterizing the phases of matter. For instance, given a finite density of particles (say, half-filling of bands) in a noninteracting equilibrium system, a gapped single-particle spectrum implies that the many-body state is characterized by correlations, which are often topological invariants of the lowest filled band. Such a direct mapping between the single-particle states and the many-body state is absent for non-Hermitian systems, given the system may not reach an equilibrium state but rather a nonequilibrium steady state at long times. Therefore, the method of conventional energy minimization to determine a many-body state is not directly applicable to a non-Hermitian system. In fact, not unlike the classical nonreciprocal transitions, it is possible that the

*ayanbanerjee@iisc.ac.in

†suraj.hegde@tu-dresden.de

‡adhip@pks.mpg.de

§awadhesh@iisc.ac.in

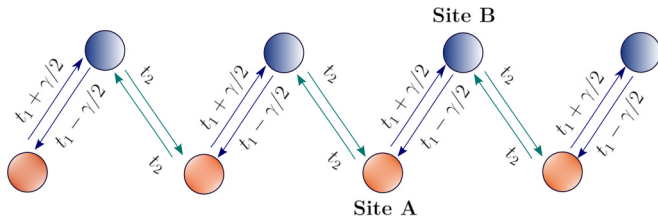


FIG. 1. Schematic of the non-Hermitian SSH model. The non-Hermitian SSH model with nonreciprocal hoppings. Intra-unit-cell hopping along the right and left are $t_1 \pm \gamma/2$, giving rise to non-Hermiticity. Inter-unit-cell hopping is fixed at t_2 .

description of the many-body state is eminent only within a set of dynamical equations rather than an underlying free energy [29].

In this work, we study such nonequilibrium steady states that arise in a concrete setting of a microscopic non-Hermitian lattice model at a finite density of fermions. The prescription to form such steady states following Refs. [10,18,19,30] is the following. Given a noninteracting Hamiltonian that has a set of single-particle eigenvalues given by $E_i = E_i^R + iE_i^I$ ($i = \{1, \dots, L\}$), a many-body state constructed out of N_p particles is a direct product of such single-particle states, with a corresponding many-body energy. Note that we use i for the square root of unity, while reserving i for the site index. There are ${}^L C_{N_p}$ number of such many-body states defined by $|\Psi_j\rangle$ with energy $\mathcal{E}_j = \mathcal{E}^R + i\mathcal{E}^I$. Each of these states evolves in time with a generalized time-evolution operator. A general many-body wave function in this Hilbert space will therefore evolve as

$$|\Psi(t)\rangle = \sum_j \psi_j |\Psi_j(t)\rangle = \sum_j \psi_j e^{-i(\mathcal{E}_j)t} |\Psi_j(t=0)\rangle. \quad (1)$$

So, any generic many-body state at late times ($t \rightarrow \infty$) will eventually evolve into the many-body eigenstate with the largest value of \mathcal{E}^I . We define this direct product state as the steady state of the system.

The model we focus on in this work is the generalization of the paradigmatic Su-Schrieffer-Heeger (SSH) Hamiltonian but with nonreciprocal hoppings to model the effect of non-Hermiticity (see Fig. 1 for a schematic). In particular, here we will discuss the physics of this system in light of the *many-body steady states* it realizes—the correlations, low-energy excitations, the entanglement signatures, and the effect of tuning the boundary conditions. Given that this is a noninteracting system, not unexpectedly, all the properties can be determined from the single-particle eigenspectrum—however, as we will show below, this steady-state interpretation and the intervening phase transitions provide insights into the nature of distinct nonequilibrium phases and their transitions in non-Hermitian quantum systems.

The choice of the nH-SSH (non-Hermitian SSH) model to illustrate this physics is most natural given the immense body of work that has been dedicated to this particular model [17,30–52]. In particular, we follow the notations introduced in Ref. [32], where a phase diagram for the nH-SSH model is presented in terms of the single-particle gap closings both for periodic and open boundary conditions, showing that the

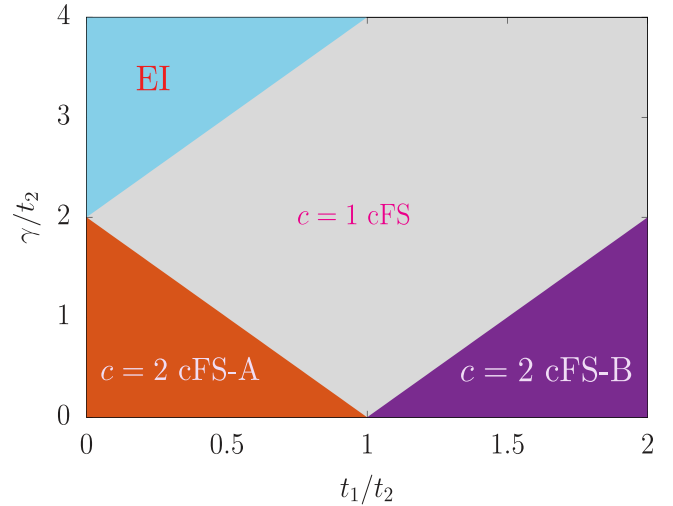


FIG. 2. Phase diagram of the non-Hermitian SSH model. The nonequilibrium phases that arise in the non-Hermitian SSH model at half-filling [see Eq. (2)] show four distinct phases. These include two central charge, $c = 2$, chiral-Fermi sea (cFS) phases (labeled A and B), one $c = 1$ cFS phase, and a non-Hermitian chiral insulating state with $c = 0$, termed an entrapped insulator (EI).

bulk-edge correspondence does not translate, in a straightforward manner, to non-Hermitian systems [53–55]. Interestingly, in Ref. [43], an interpretation for the appearance of boundary modes and the related non-Hermitian skin effect was understood within the framework of a generalized Brillouin zone, while in Ref. [36] such a correspondence was seen with bulk biorthogonal polarization. In this work, we revisit this problem in terms of the many-body steady states that the system realizes. We find four distinct nonequilibrium phases with characteristic currents, low-energy excitations, correlations, and entanglement signatures. We provide a comprehensive understanding of these nonequilibrium phases and the nature of the transitions between them. We further discuss the effects of weakening the boundary term, such that topological boundary modes appear in these steady states. We further point out various connections between this many-body perspective and the single-particle dispersion framework discussed previously in the literature [32].

The central finding of this work is presented in Fig. 2, where we show that by varying the parameters characterizing the nH-SSH model—(a) t_1/t_2 , the dimerization scale and (b) γ/t_2 , the nonreciprocal intra-unit-cell hopping (see Fig. 1)—one can access four distinct nonequilibrium phases: (i) a chiral metal with central charge 2 (A) ($c = 2$ cFS-A), (ii) a chiral metal with central charge 1 ($c = 1$ cFS), (iii) another chiral metal with central charge 2 ($c = 2$ cFS-B), and (iv) an entrapped insulator EI ($c = 0$). Our work, even while uncovering the different nonequilibrium many-body steady states in this model system—also provides qualitative descriptions of physically relevant quantities in each of them, which may be experimentally accessible. In this respect, our study fills the crucial gap between the many studies focusing on the single-particle spectrum and their implications on a many-body state as realized in a non-Hermitian system. Interestingly, as in Hermitian systems, band descriptions here play a crucial role in

the properties of the non-Hermitian many-body phase, albeit with remarkably different features such as the existence of chiral Fermi seas, steady-state currents, and leaky boundary modes.

In the rest of the paper, we discuss the physics underlying these phases. In Sec. II we introduce the Hamiltonian and discuss its symmetries. In Sec. III we present the methodology and introduce various diagnostic tools to characterize these phases. In Sec. IV we explore the emergence of these four distinct phases and their properties and connections to spectral topology, as well as their low-energy theories. In Sec. V we examine the effect of tuning the boundary conditions from periodic to open and the realization of leaky boundary modes. Finally, in Sec. VI we summarize our results and present an outlook.

II. NON-HERMITIAN SSH MODEL

A. Model

The Hamiltonian of interest for the nH-SSH model is given by [32] (also called the “chiral nH-SSH” model; see, for example, Ref. [33])

$$H = - \sum_i [t_1 (c_{i,A}^\dagger c_{i,B} + \text{H.c.}) + t_2 (c_{i+1,A}^\dagger c_{i,B} + \text{H.c.})] + \sum_i \frac{\gamma}{2} (c_{i,B}^\dagger c_{i,A} - c_{i,A}^\dagger c_{i,B}), \quad (2)$$

where $c_{i,\alpha}^\dagger$ ($c_{i,\alpha}$) is the fermionic creation (annihilation) operator at site i for sublattice $\alpha = A, B$ (see Fig. 1). The intra- and inter-unit-cell hopping amplitudes are given by t_1 and t_2 , respectively, and γ introduces a nonreciprocity only in the intra-unit-cell hopping, thereby introducing non-Hermiticity in the system. We consider t_1, t_2, γ to be real-valued. Moving to k -space by Fourier transforming the operators [using $c_{k,A}^\dagger = \frac{1}{\sqrt{L}} \sum_i \exp(-ik_i) c_{i,A}^\dagger$], we obtain

$$H(k) = \mathbf{d}(k) \cdot \boldsymbol{\sigma} = \begin{bmatrix} 0 & t_2 e^{-ik} + t_1 - \gamma/2 \\ t_2 e^{ik} + t_1 + \gamma/2 & 0 \end{bmatrix}, \quad (3)$$

where $\mathbf{d}(k) \equiv (d_1, d_2, d_3) = (t_1 + t_2 \cos k, t_2 \sin k - i\gamma/2, 0)$, and $\boldsymbol{\sigma}$ is the triad of Pauli matrices. The eigenvalues of $H(k)$ are given by $E_k = \pm d(k)$, where

$$d(k) = \pm \sqrt{t_1^2 + t_2^2 - \gamma^2/4 + 2t_1 t_2 \cos k - i t_2 \gamma \sin k}. \quad (4)$$

The right eigenvectors [corresponding to $\pm d(k)$ energy] are of the form

$$|\psi^\pm\rangle = \frac{1}{\sqrt{1 + |a|^2}} \begin{pmatrix} a \\ \pm 1 \end{pmatrix}, \quad (5)$$

where

$$a = -\sqrt{\frac{t_1 + t_2 e^{-ik} - \gamma/2}{t_1 + t_2 e^{ik} + \gamma/2}}. \quad (6)$$

The Hamiltonian has a sublattice symmetry $\mathcal{S} : c_{iA} \rightarrow -c_{iA}^\dagger, c_{iB} \rightarrow c_{iB}^\dagger$ ($\mathcal{S} H^\dagger \mathcal{S}^{-1} = H$), $\sigma_z H(k) \sigma_z^{-1} = -H(k)$ [24].

B. Single-particle eigenvalues and spectral topology

The nH-SSH model has been studied extensively. Here we briefly summarize the main results (see, for example, Refs. [19,32]). The single-particle spectrum shows gap closings (for absolute values of energies) for lines $\gamma = 2(t_1 \pm 1)$ and $\gamma = 2(1 - t_1)$ dividing the phase diagram into four regions (see Fig. 2): (i) $\gamma < 2(1 - t_1)$ —the complex spectrum when plotted in the complex plane $\{\text{Re}[E], \text{Im}[E]\}$ is comprised of two spectral lobes separated in real energy by a line gap [20,24,42] [see Fig. 3(a)]; (ii) $t_1 > 1 + \gamma/2$ —spectral topology is again similar to (i) [see Fig. 3(a)]; (iii) $\gamma > 2(1 - t_1), \gamma < 2(1 + t_1)$ —the spectral topology is that of a single loop in the complex plane [see Fig. 3(b)]; and (iv) $\gamma > 2(1 + t_1)$ —the complex spectrum has a two-lobe structure with the lobes vertically displaced along the imaginary axis [see Fig. 3(c)]. Since the transition between the various phases in Fig. 2 occurs as the spectral topology of the complex spectrum also changes (see Fig. 3), the transitions are marked via a gap closing in both real and imaginary eigenvalue directions.

The spectral topology can be characterized by the winding number w [24],

$$w = \int_{-\pi}^{\pi} \frac{dk}{2\pi i} \partial_k (\ln (\det[H(k) - E_B])), \quad (7)$$

where E_B is some base energy. Immediately, the four regions [(i)–(iv)] are characterized by winding numbers $(1, 1, 1/2, 0)$ [20,24,42], respectively. Interestingly, these winding numbers have a one-to-one correspondence with nondecaying chiral modes, as we briefly discuss next.

Each of the single-particle states is associated with a current determined by the group velocity ($\sim \frac{d \text{Re}[E_k]}{dk}$) and a lifetime given by the inverse of the imaginary part of the energy eigenvalue $\text{Im}[E_k]$. This immediately shows the existence of chiral modes that decay/grow in the single-particle spectrum (see Fig. 3). In an equilibrium system, such modes are stationary states at equal energy, which guarantees that any equilibrium state cannot have a finite current (this follows from the celebrated Nielsen-Ninomiya theorem [56]). However, in a nonequilibrium setting, such as here, these chiral modes have an imaginary part of the energy eigenvalue of opposite sign, which means that at long times only one can be populated, leading to steady states that can carry a finite current [57]. In fact, the existence of such chiral modes and the finite winding numbers are interrelated, symmetry-protected, and guaranteed via the properties of the spectral topology [24,58,59]. Having discussed the properties of the nH-SSH model using its single-particle spectrum and its properties, we next delve into the discussion of the many-body states obtained here at a *finite filling*.

III. METHODOLOGY

In this section, we briefly discuss our method for construction of steady states at finite filling, and we define quantities of interest such as current and correlation functions in these steady states.

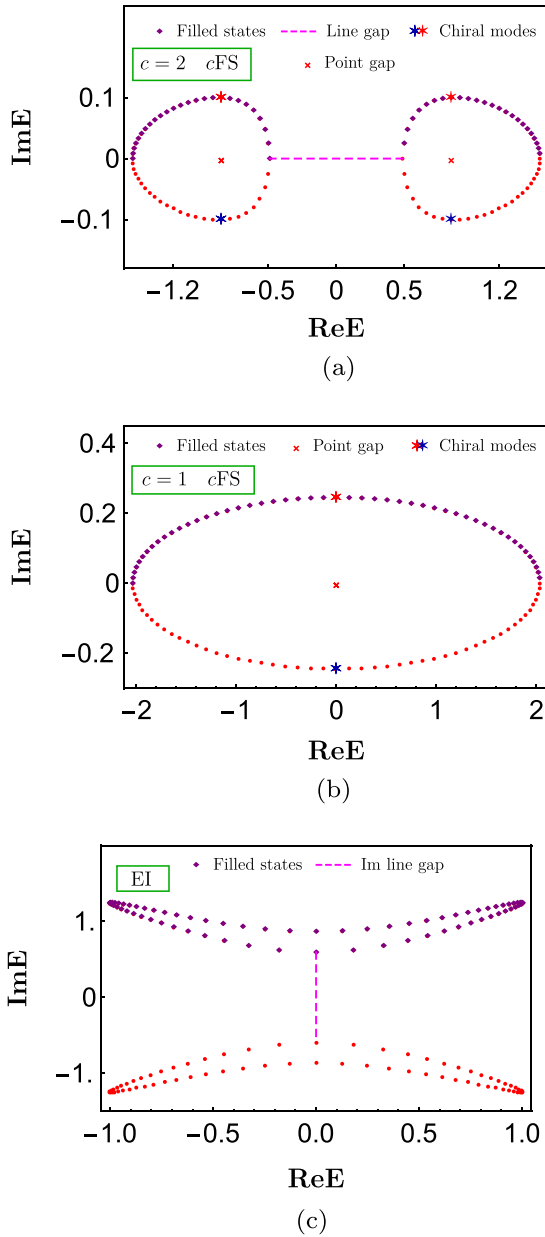


FIG. 3. Nature of the complex eigenspectrum. The real and imaginary parts of the single-particle energy eigenvalues are shown in (a) $c = 2$ cFS-A ($t_1 = 0.5$ and $\gamma = 0.2$) with two spectral loops separated by a real line gap, (b) $c = 1$ cFS ($t_1 = 1.05$ and $\gamma = 0.5$), which has a single loop, and in (c) the entrapped insulator phase ($t_1 = 0.1$ and $\gamma = 2.5$), which has two loops but separated by an imaginary line gap. The purple diamonds denote the filled states at half-filling, while the red (blue) stars show growing (decaying) chiral modes. The dotted lines (crosses) indicate the line gap (point gaps). Here, t_1 and γ are scaled in terms of t_2 . We stick to this convention unless otherwise specified.

A quadratic non-Hermitian Hamiltonian of the form $\mathcal{H} = \Psi^\dagger H \Psi$ is diagonalized using $H = U_R \Lambda U_R^{-1}$, where

$$\tilde{c}_i^\dagger \equiv \sum_{j=1}^L (U_R)_{ji} c_j^\dagger, \quad \tilde{c}_i \equiv \sum_{j=1}^L (U_R^{-1})_{ij} c_j, \quad (8)$$

and c_j^\dagger (c_j) are the fermionic creation (annihilation) operators defined at site j such that $\mathcal{H} = \sum_i E_i \tilde{c}_i^\dagger \tilde{c}_i$, where $E_i = E_i^R + iE_i^I$, and E_i^R and E_i^I are the real and imaginary parts, respectively, of every eigenvalue E_i . Note that $(\tilde{c}_i)^\dagger \neq \tilde{c}_i^\dagger$, since this is a biorthonormal basis. These operators satisfy the conventional fermionic algebra $\{\tilde{c}_i^\dagger, \tilde{c}_j\} = \{c_k^\dagger, c_l\} = \delta_{ij}$ and $\{\tilde{c}_i^\dagger, \tilde{c}_j^\dagger\} = \{c_k^\dagger, c_l^\dagger\} = 0$, such that any particle number state with N_p particles,

$$|\Psi_\alpha\rangle = \tilde{c}_{i_1}^\dagger \tilde{c}_{i_2}^\dagger \cdots \tilde{c}_{i_{N_p-1}}^\dagger \tilde{c}_{i_{N_p}}^\dagger |\Omega\rangle, \quad (9)$$

has a well-defined many-body energy $\mathcal{H}|\Psi_\alpha\rangle = (\sum_{j=1}^{N_p} E_{i_j} \equiv \mathcal{E}_\alpha)|\Psi_\alpha\rangle$ that evolves in time as

$$|\Psi_\alpha(t)\rangle = e^{-i(\mathcal{E}_\alpha)t} |\Psi_\alpha(t=0)\rangle. \quad (10)$$

Given the nonunitary nature of evolution, such a many-body state needs to be renormalized during the time evolution [60]. The state that grows the fastest is given by the maximum value of \mathcal{E}_α^I . Therefore, at long times, the steady state of the system is defined as the one that has the largest value of \mathcal{E}_α^I . Any other many-body state ($|\Psi_{\alpha'}\rangle$) with energy $\mathcal{E}_{\alpha'}^R + i\mathcal{E}_{\alpha'}^I$ has a real gap $\Delta_{\alpha\alpha'}^R = \mathcal{E}_{\alpha'}^R - \mathcal{E}_\alpha^R$ and similarly an imaginary gap as $\Delta_{\alpha\alpha'}^I = \mathcal{E}_{\alpha'}^I - \mathcal{E}_\alpha^I$. The latter also defines the lifetime of the α' state $\equiv \frac{1}{\Delta_{\alpha\alpha'}^I}$ for the excitation to decay into the steady state. Applying this for the nH-SSH model, we calculate the following quantities.

A. Current response

The current in any system is the response of the Hamiltonian to an external gauge field. Threading a small flux ϕ [$t_2 \rightarrow t_2 e^{i\phi}$] through a one-dimensional ring [see Eq. (2)] leads to the current operator as

$$J = \lim_{\phi \rightarrow 0} -L \frac{\partial H(\phi)}{\partial \phi} = -i \sum_i (t_2 c_{i+1,A}^\dagger c_{i,B} - t_2 c_{i,B}^\dagger c_{i+1,A}). \quad (11)$$

When Fourier-transformed [using $c_{k,A}^\dagger = \frac{1}{\sqrt{L}} \sum_i \exp(-ik i) c_{i,A}^\dagger$], the operator becomes

$$J = \sum_k (i e^{ik} c_{k,A}^\dagger c_{k,B} - i e^{-ik} c_{k,B}^\dagger c_{k,A}). \quad (12)$$

When evaluated on a single-particle state $|\psi^\pm\rangle$ [see Eq. (5)], one obtains

$$j_{k\pm} = \pm \frac{i}{2L} (-e^{-ik}/a + e^{ik}a). \quad (13)$$

For a filled state, depending on the occupied states, one can therefore straightforwardly calculate the total current, which is an integral over the corresponding region of the Brillouin zone.

The total current J can be equivalently expressed as follows:

$$J = \int_0^{2\pi} n(E_k) \langle j_k \rangle dk = \oint n(E_k) dE_k, \quad (14)$$

where the integral is over the spectral loop in the complex energy plane, and $n(E_k)$ is an effective distribution function

that defines which states are occupied [61]. Therefore, the way the steady states are formed here is to consider a distribution function of the kind

$$n(E_k) = \frac{1}{1 + \exp(-\beta(\text{Im}[E_k] - \mu))}, \quad (15)$$

where $\beta = 1/T$ and μ is the chemical potential, which is set to zero for the half-filled case.

B. Correlation functions

Given the occupancy of the single-particle states, the correlation functions are given by

$$C^{B,A}(r) = \frac{1}{L} \sum_k \frac{1}{2a} e^{-ikr} (n_{k+} - n_{k-}), \quad (16)$$

$$C^{A,B}(r) = \frac{1}{L} \sum_k \frac{a}{2} e^{-ikr} (n_{k+} - n_{k-}), \quad (17)$$

$$C^{A,A}(r) = \frac{1}{L} \sum_k \frac{1}{2} e^{-ikr} (n_{k+} + n_{k-}), \quad (18)$$

where $n_{k\pm}$ are the occupations of the \pm bands.

C. Entanglement

Having calculated the correlators, it is straightforward to evaluate the entanglement entropy, S_l , of a subsystem of length (l) [62]. The eigenvalues of the subsystem-limited correlator matrix ($\equiv e_i$) are related to the subsystem entanglement entropy via

$$S_l = - \sum_i (e_i \ln(e_i) + (1 - e_i) \ln(1 - e_i)). \quad (19)$$

Having discussed the various quantities of interest, we next investigate the various nonequilibrium phases realized in the nH-SSH model.

IV. NONEQUILIBRIUM PHASES AND THEIR TRANSITIONS

The nonequilibrium phase diagram as a function of t_1/t_2 and γ/t_2 that we obtain is shown in Fig. 2. We discover four distinct nonequilibrium phases, which we describe below. Before introducing the non-Hermiticity parameter γ , let us briefly recall the phases that arise as a function of t_1 at $\gamma = 0$.

A. $\gamma = 0$ limit

At $\gamma = 0$ for both $t_1 < t_2$ and $t_1 > t_2$ one has gapped phases, which have a bond dimerlike order. The fermion-fermion correlator decays exponentially with a functional form $C_{i,j} \sim e^{-r/\xi}$, where ξ is the correlation length ($\xi^{-1} = \frac{1}{2} |\ln \frac{t_1}{t_2}|$) [63]. At $t_1 = t_2$, there exists a gapless point, which corresponds to a free Fermi sea that has two linearly dispersing Dirac fermions at $k = \frac{\pi}{2}$ and $\frac{3\pi}{2}$ (for a single-site unit cell, the same points change to $k = 0, 2\pi$ for a two-site unit cell due to Brillouin zone folding), rendering it a critical theory with central charge $c = 1$. We now discuss the effects of including non-Hermiticity and the phases that emerge.

B. $c = 2$ chiral metal (CFS-A)

The first nontrivial phase arises when we have both $t_1 < t_2$ and $\gamma < t_2$. The Hermitian system at ($t_1 \sim 0, \gamma = 0$) exhibits two nearly flat bands, one of which is fully filled in equilibrium. Even a perturbatively small γ immediately leads to a finite imaginary part of the energy eigenvalues [see Fig. 4(a)], which makes the equilibrium state unstable and takes the many-body state to a unique steady state that has a finite current. It is in this sense that the non-Hermitian limit of the system is *not* perturbatively connected to the Hermitian physics. Not unlike the Hatano-Nelson model, where the system stabilizes a steady state with a Galilean boosted Fermi sea, here the Hermitian band insulator splits into two Fermi seas occupying the two bands (orange and green), respectively, from $\pi < k < 2\pi$ (orange band) and from $0 < k < \pi$ (green) [see Fig. 4(a)].

Nature of the steady state: It is interesting to note that exactly at $\gamma = 0$, the system has only the lower band filled. Inclusion of any finite γ provides a timescale $\tau_{k,n} = \frac{1}{E_{k,n}^I}$ to each of the states after which the state grows (decays) given $E_{k,n}^I > 0$ ($E_{k,n}^I < 0$). Interestingly, every band chooses both signs for $E_{k,n}^I$, therefore while the occupation of the lower band from $0 < k < \pi$ is stable, at long times the system moves to a steady state where the particles occupy the higher (real) energy band between $0 < k < \pi$ (see Fig. 5).

An illustrative way of seeing this is to plot the single-particle spectrum in the complex plane, which shows two closed spectral loops [see Fig. 6 (top panel)]. These loops have a finite winding with a width Δ_r along the real axis. In the $\gamma = 0$ limit this corresponds to the dispersing width of each of the bands. The loops are further separated in real energy by a “band” gap of Δ_{bg} (also called a line gap). The complete bandwidth of the spectrum along the real axis is Δ_{bw} .

The existence of the spectral loops is symmetry-protected, which guarantees the existence of a state with complex energy $-E$ given a state with energy E . Given the existence of four eigenvalues that have a zero imaginary component, at half-filling, the system has *six* many-body states that have the same total imaginary component while different values of the real component. Therefore, both the spectral winding and the number of steady states in the system are intricately related. The nonequilibrium steady state (NESS) corresponds to the minimum total real energy and the maximum total imaginary component characterized by a split Fermi sea on both the lower and the upper band (see Fig. 6) and four Fermi points.

Excitations: The NESS can excite into five other steady states (cFS^{(1)–(5)}) via particle-hole excitations, which leads to states that have the same total imaginary component, however having a gap in real energies determined by Δ_r and Δ_{bw} [see Fig. 6 (bottom)]. These excitations *do not decay* and can have finite amplitudes at long times. Each of these multiple steady states has an indistinguishable current and real-space correlations. However, these steady states themselves are *gapless* and are dominated by particle-hole excitations within the spectral loops, which, in turn, are characterized by point gaps in the complex energy plane. Given the continuum of excitations within each loop, these excitations live longer the closer they are to the Fermi points.

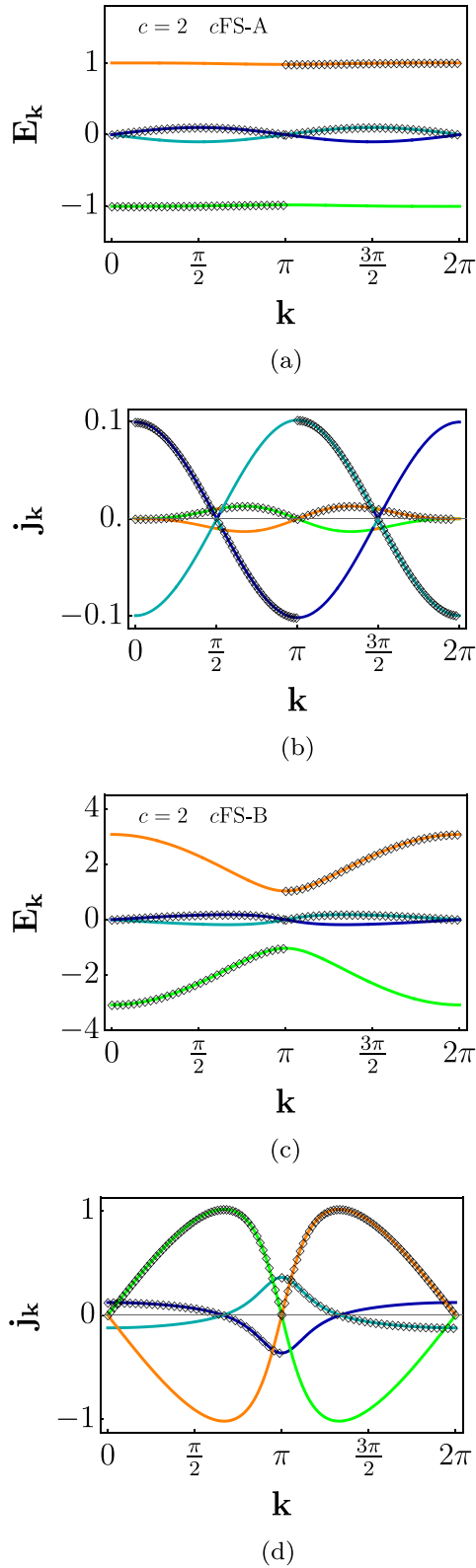


FIG. 4. Single-particle dispersion and currents of $c = 2$ chiral metals. The real (orange-green lines) and imaginary parts (cyan-blue lines) of the eigenspectrum and single-particle current [see Eq. (13)] as a function of k for various parameters are shown. In (a), (b) $t_1 = 0.01$, $\gamma = 0.2$ ($c = 2$ cFS-A). In (c), (d) $t_1 = 2.1$, $\gamma = 0.75$ ($c = 2$ cFS-B). For half-filling, the occupied k points are further highlighted by black diamonds.

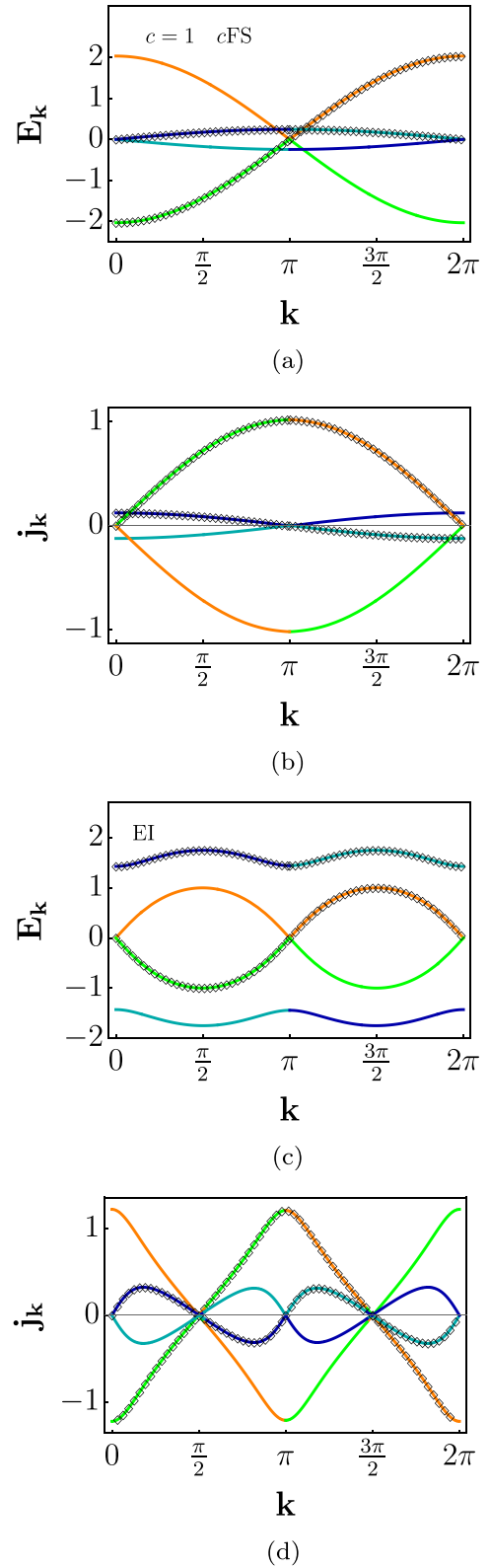


FIG. 5. Single-particle dispersions and currents of $c = 1$ cFS and $c = 0$ EI. The real (orange-green lines) and imaginary parts (cyan-blue lines) of the eigenspectrum and single-particle current [see Eq. (13)] as a function of k for various parameters are shown. In (a), (b) $t_1 = 1.05$, $\gamma = 0.5$ ($c = 1$ cFS), and (c), (d) $t_1 = 0.01$, $\gamma = 3.5$ (EI). For half-filling, the occupied k points are further highlighted by black diamonds.

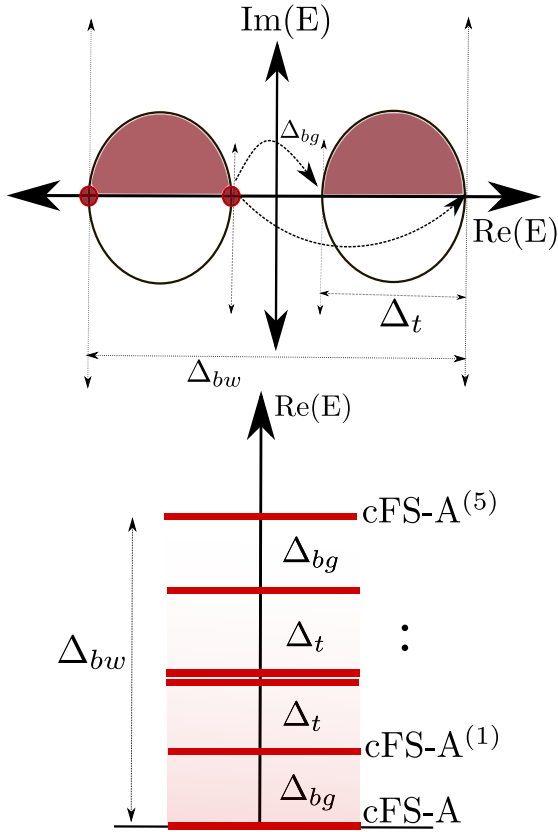


FIG. 6. Steady state and the nature of excitations in the chiral FS (A) phase. A schematic showing the steady state as well as excitations in the cFS-A phase (see Sec. IV B). The spectral loops of width Δ_t (top) are separated by a line gap Δ_{bg} for a system of total bandwidth Δ_{bw} . At half-filling, six steady states exist (cFS - $A^{-(5)}$), which are separated in real energies due to particle-hole excitations (shown using arrows). The six steady states are shown below.

Current: The occupied bands in the system lead to a finite current for the NESS, given that the single-particle states are current-carrying states and they contribute additively to the many-body state. This is in contrast with any Hermitian system where current contributions from various single-particle states cancel pairwise, leading to an equilibrium state with zero current. For instance, here both the $+$ band and the $-$ bands have a positive contribution to the current [see Fig. 4(b)]. It is easy to integrate $j_{k\alpha}$ to find the total current in the system, even when γ is perturbatively small. This finite current

$$j_o = \frac{2}{\pi} t_1 \quad (20)$$

is characteristic of the NESS. Nonzero γ leads to a quadratic increase [see Fig. 7(a)]

$$J_{|\gamma|>\epsilon, \epsilon \rightarrow 0} \sim \text{sgn}(\gamma) \frac{2t_1}{\pi} \left(1 + \frac{3}{25} \gamma^2 \right). \quad (21)$$

In fact, the same behavior is expected for all six steady states in the system, given that the current is determined collectively by the bulk of the single-particle states.

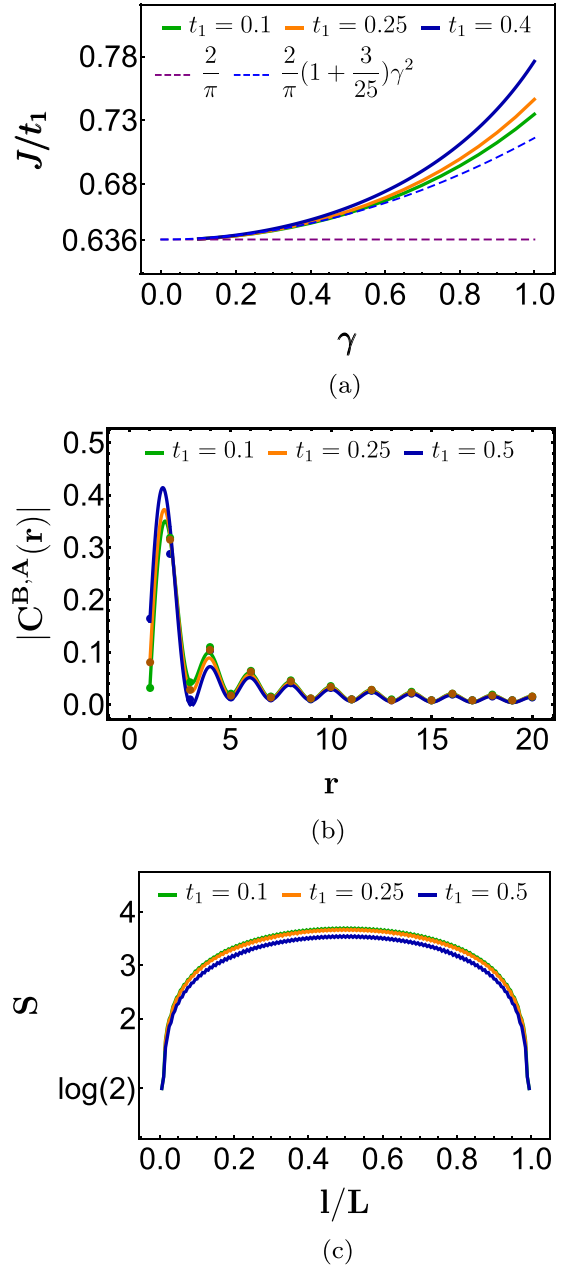


FIG. 7. Nature of $c = 2$ cFS-A. (a) The behavior of chiral current, for three different values of t_1 , as a function of the non-Hermitian coefficient γ [see Eq. (21)]. (b) The correlator, $C_{B,A}(r)$, as a function of r at $\gamma = 0.5$ for different values of t_1 . The numerical values from real-space calculation are the points ($L = 300$). The continuous lines are the expressions shown in Eq. (23) for appropriate parameters. (c) Entanglement entropy for three different values of t_1 as a function of l/L for $L = 300$.

Let us stress that the origin of this finite current in the NESS is purely topological in nature. A finite winding of $H(k)$ around any reference point in the complex spectral plane ensures the existence of a finite additive current from various single-particle states, as seen in Eq. (14) [61]. In the cFS-A phase, the current contributions stem from the winding of the two spectral loops. While the spectral topology of the Hamiltonian gives rise to finite current, the notion of steady-state

filling ensures a purely real total current through cancellation of all imaginary parts [see Fig. 4(b)].

Correlations: Having discussed the current-carrying nature of this state, it is natural to pose the question regarding how the fermions are mutually correlated. It is interesting to note that even while the fermions at the same sublattice are uncorrelated, i.e.,

$$C^{A,A}(r) = C^{B,B}(r) = \frac{1}{2}\delta(r), \quad (22)$$

the fermions on two different sublattices are power-law correlated (to a leading-order dependence on γ),

$$C^{A,B}(r) \sim \frac{\gamma}{r} \sin\left(\frac{\Delta k_F r}{2}\right), \quad (23)$$

with characteristic oscillations governed by a finite density of fermions in each band ($\Delta k_F = \pi$). This γ -dependent behavior is in addition to a γ -independent power law with similar oscillations. This is in direct contrast with the Hermitian limit of a band insulator where each of these correlators falls exponentially with distance [see Fig. 7(b)]. It is also important to note that generally for a non-Hermitian system, $\langle c_i^\dagger c_j \rangle \neq [\langle c_j^\dagger c_i \rangle]^\dagger$. The above features, therefore, qualify that this non-Hermitian phase is in fact a chiral-metal.

Entanglement: We next focus on the entanglement properties of this phase, where a part of the system under consideration in real space (l) is traced over, and the entanglement of the remaining part is calculated. Given the noninteracting system, we use the prescription given by Peschel and Calabrese [21,63,64] and extract the central charge of the system using (for periodic boundary conditions)

$$S = \frac{c}{3} \ln \left[\frac{L}{\pi} \sin \left(\frac{\pi l}{L} \right) \right], \quad (24)$$

where we find that $c = 2$ [see Fig. 7(c)]. This is consistent with the fact that the system behaves like two disjoint Fermi surfaces (corresponding to two bands) with a Fermi volume of π , and therefore gapless low-energy excitations on four Fermi points, where each potentially contributes $c = \frac{1}{2}$ to the central charge.

Away from half-filling: All of the discussion above made use of the fact that we keep the non-Hermitian system at a finite density of fermions that is fixed to *half*. This implicitly assumes that even while single-particle states themselves can decay, the system pumps in new particles to maintain a finite filling. However, a finite current is rooted in the spectral topology, and the filling only changes the contribution of single-particle states to the total current. Away from half-filling, the nature of the metallic state does not change, since both bands still get partially but equally filled, the four Fermi points still remain, and correlations are still power law, albeit with a different wavelength of oscillation, which, in turn, corresponds to the changing Fermi volume. However, the value of the steady-state current is density-dependent and follows a behavior characteristic of exclusion processes $\sim \rho(1 - \rho)$ (see, for example, Ref. [65]), as seen in Fig. 8. In this way, it lends credence to the ideas of non-Hermitian systems modeling either open systems or boundaries of higher-dimensional symmetry-protected topological systems [58], where the boundary states are maintained at a finite filling even while the system is connected to the leads.

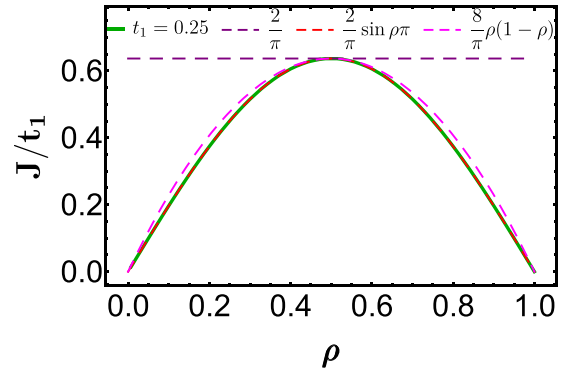


FIG. 8. Steady-state current in cFS-A phase. Steady-state current, J , as a function of density, ρ , at $t_1 = 0.25$ in the cFS-A phase. Note the behavior characteristic of exclusion processes with a maximum at half-filling. Here we set $\gamma = 0.1$.

C. $c = 1$ chiral metal (cFS)

There exists another distinct chiral metallic phase in this system with two Fermi points. As we show below, this phase is smoothly connected to the Hatano-Nelson steady state, which is realized in the celebrated single-band nonreciprocal hopping Hamiltonian [66]. The ground state of $t_1 = t_2$, $\gamma = 0$ point is a half-filled Fermi sea with two Fermi points. Any nonreciprocal hopping immediately shifts the Fermi sea to a finite-momentum current-carrying steady state still with two Fermi points, and gapless excitations [Figs. 5(a) and 5(b)]. While at $\gamma = 0$ this phase is unstable to dimerization, a finite γ opens up a window where even upon the introduction of dimerization ($t_1 \neq t_2$) the chiral metallic phase continues to remain stable. We next discuss the properties of this phase.

Nature of steady state and excitations: At $\gamma = 0$, the complex spectrum is a single continuous line that spans the total bandwidth. The equilibrium state at half-filling is given by occupation of all single-particle states with $\text{Re}[E] < 0$. Introduction of a nonzero γ adds an imaginary component to the single-particle eigenvalues, which leads to single loop in the complex spectrum (see Fig. 3). The existence of two eigenvalues with zero imaginary component leads to two steady states that are separated in real energy by their bandwidth Δ_{bw} . Each of these states, however, has a set of gapless excitations that decay with time.

Current and correlations: In this phase, both of the steady states carry a finite current (see Fig. 9), where the current is given by

$$J \sim \text{sgn}(\gamma) \frac{2t_1}{\pi} \left[1 - \frac{\gamma^2}{16} \right]. \quad (25)$$

The current comes from the finite winding of a single loop in the complex spectral plane. As is expected of a gapless state, the fermionic correlations decay in a power-law fashion and the existence of a single Fermi surface with a Fermi volume of 2π leads to no characteristic oscillations in the intersublattice correlator such that even while $C^{A,A}(r) = C^{B,B}(r) = \frac{1}{2}\delta(r)$, one finds the leading-order dependence on γ as

$$C^{A,B}(r) \sim \frac{\gamma}{r}, \quad (26)$$

which again is in addition to a γ -independent power-law part.

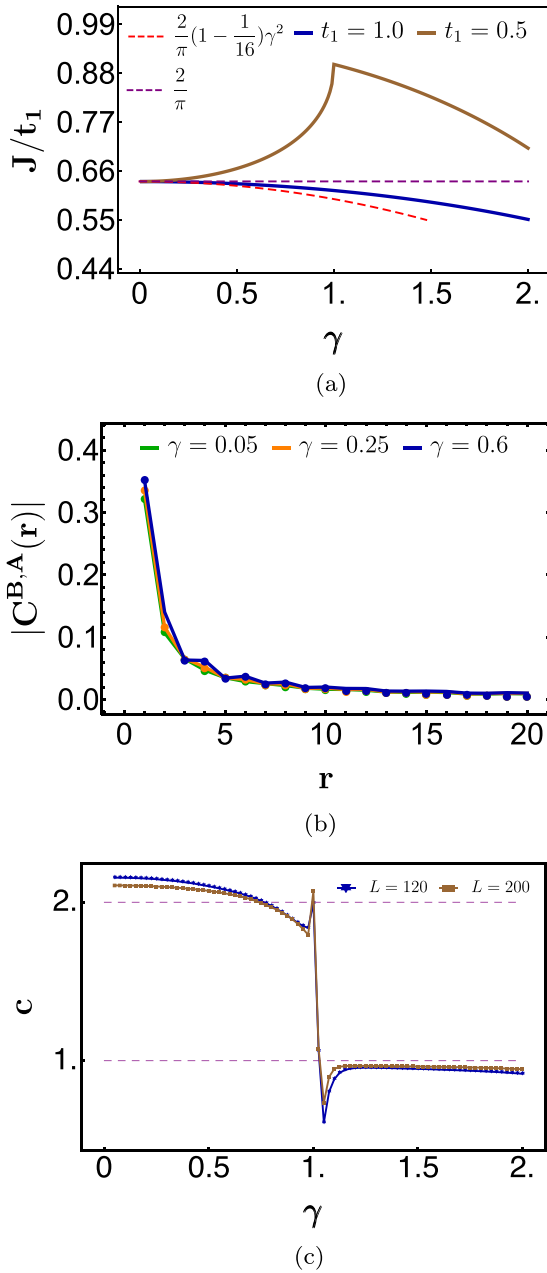


FIG. 9. Many-body properties of $c = 1$ cFS. (a) Chiral current for two different values of t_1 , as a function of the non-Hermitian coefficient γ [see Eq. (25)]. (b) The correlator, $C_{B,A}(r)$, as a function of r for $t_1 = 1.0$ for different values of γ . The numerical values from real-space calculation are the points ($L = 300$). The continuous lines are the expressions shown in Eq. (26) for appropriate parameters. (c) The central charge variation is shown as a function γ ($t_1 = 0.5$) for two system sizes. The nonanalytic behavior in the current and the central charge arise at $t_1 = 0.5$ due to cFS-A to $c = 1$ cFS transition.

Entanglement and density dependence: Given two Fermi points, we find $c = 1$ from the subsystem entanglement scaling (see Fig. 9), characterizing the phase as a $c = 1$ chiral metal. Going away from half-filling again leads to a change in the current density, additionally resulting in oscillations in

the correlators characteristic of the reduced Fermi volume (not shown).

D. Entrapped band insulator

A novel nonequilibrium phase of matter that is realized here is that of an entrapped insulator (EI) which gets stabilized for the $\gamma/t_2 > 2(t_1/t_2 + 1)$ region of the phase diagram (see Fig. 2). One illustrative limit to start from is $t_2 = 0$ ($t_1 \rightarrow \infty$) and $\gamma \neq 0$, where the chain breaks into a sequence of dimer states, albeit with strong nonreciprocal coupling within each dimer. At exactly half-filling, each unit cell can host a single electron stabilizing a non-Hermitian insulating state. Given that every particle is dynamically trapped in a unit cell with a finite intra-unit-cell current, we call this new state an EI. However, the inter-unit-cell current remains zero. It is this phase that continues to remain stable for large values of γ and a window of t_1 and t_2 regions.

Nature of the steady state: The complex spectrum again shows a two-lobe structure with a line gap in this phase, however the line gap now exists in the imaginary eigenvalue direction (see Fig. 3). At half-filling, the upper lobe is completely filled creating a gap to excitations that are short-lived with a finite lifetime.

Current and correlations: Given the gapped character of the system, this steady state has zero current [Figs. 5(c) and 5(d)]. This is also seen through the fact that the spectral loop in this case has zero winding. The intersublattice fermion correlator decays exponentially with a form given by

$$C^{A,B}(r) \sim \exp(-r/\xi), \quad (27)$$

where $\xi \approx 1/\gamma$ (see Fig. 10).

Entanglement: The bipartite entanglement entropy as a function of subsystem size shows characteristic oscillations with periodicity of two sites signaling a dimer order with a value $\sim \log(2)$ when the partition is intra-unit-cell, and ~ 0 when the partition is inter-unit-cell (see Fig. 10). One finds the inter-unit-cell entropy to be negative for larger values of t_1 , as has been reported in other non-Hermitian systems [64], however its interpretation in terms of information is not clear at present and merits further investigation.

E. $c = 2$ chiral metal (cFS-B)

We now briefly discuss another chiral metallic phase that appears when $t_1 \gg t_2$. While many of the essential properties of this phase are similar to cFS-A, one distinctive feature is the orbital character of the steady state, which we discuss next.

At $\gamma = 0$ the $t_1 > t_2$ and $t_1 < t_2$ phases are both insulating with a band gap, however the orbital character of the bands is distinct [67]. For instance, for $t_1 < t_2$ the half-filled equilibrium state has a distinct polarization compared to $t_1 > t_2$, which is reflected in a winding number that changes discontinuously at $t_1 = t_2$ [26,27,68]. Nonzero γ does not change the orbital character of the single-particle bands in the $\gamma = 0$ limit. For instance, decomposing the band wave functions ($n = 0, 1$) into the bonding (antibonding) contributions ($c_{nk}^\dagger = \psi_{\alpha k}^\dagger c_{k\alpha}^\dagger + \psi_{\beta k}^\dagger c_{k\beta}^\dagger$), where $c_{k\alpha}^\dagger = \frac{1}{\sqrt{2}}(c_{kA}^\dagger + c_{kB}^\dagger)$ and $c_{k\beta}^\dagger = \frac{1}{\sqrt{2}}(c_{kA}^\dagger - c_{kB}^\dagger)$, shows the characteristic twist of the bands when $t_1 < t_2$ (when $\gamma \neq 0$)

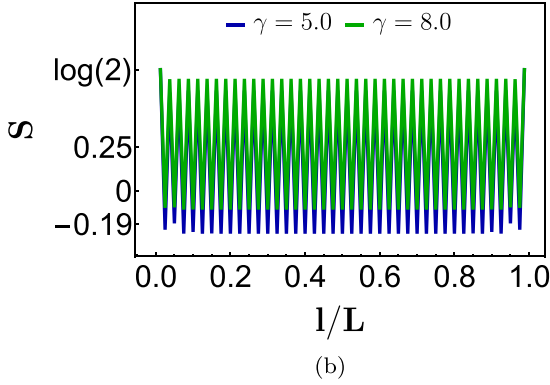
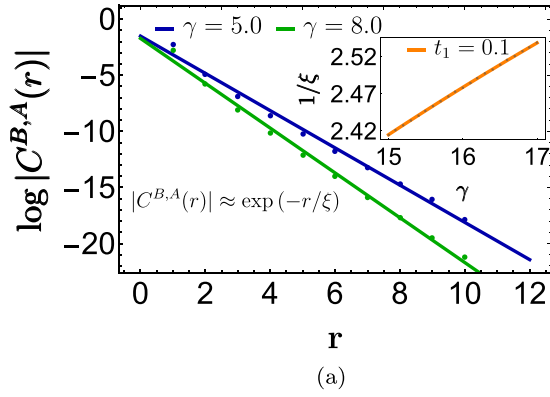


FIG. 10. Many-body properties of $c = 0$ EI. (a) The correlator $C_{B,A}(r)$ in logarithmic scale as a function of r for different values of γ . The numerical values from real-space calculation are the points ($L = 300$). The continuous lines are the expressions shown in Eq. (27) for appropriate parameters. (b) Entanglement entropy for different parameter values of γ , as a function of l/L . Here, we have set $t_1 = 0.1$.

when $|\psi_{\alpha k}^n|^2$ is plotted for both bands (see Fig. 11). The introduction of non-Hermitian instability due to γ leads to half-filling of both of these bands (therefore maximizing the total imaginary component) for the steady state.

Moreover, the current in the system is dominated by the lower hopping scale, which is $t_2 = 1$ in the regime when $t_1 > t_2$. Therefore, the current in cFS-B starts at $2/\pi$ when $\gamma \rightarrow 0$ and is independent of the value of t_1 (see Fig. 12).

F. Low-energy theories and the nature of phase transitions

Having discussed the character of the steady states and their low-energy excitations, we now discuss the nature of these phase transitions between various chiral metals and entrapped insulating states (Fig. 13). We note that a conventional energy minimization to find the ground state or the excitations is not sufficient to describe the steady states. Therefore, one needs to go beyond the conventional paradigm to describe such phase transitions, as we will see next.

1. Hatano-Nelson model and $c = 1$ cFS

The Hatano-Nelson Hamiltonian is given by [66]

$$H_{\text{HN}} = \sum_i -t(c_i^\dagger c_{i+1} + \text{H.c.}) + \gamma(c_i^\dagger c_{i+1} - \text{H.c.}), \quad (28)$$

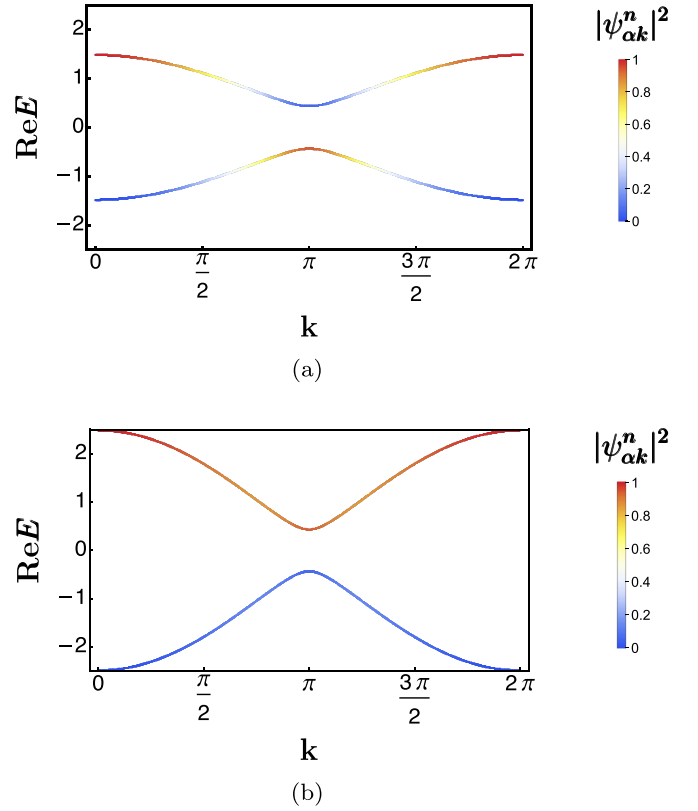


FIG. 11. Distinction between two chiral phases cFS-A and cFS-B through orbital band character. The real part of the dispersion is shown with $|\psi_{\alpha k}^n|^2$ contribution in color (see Sec. IV E) with (a) $t_1 = 0.5$ and $\gamma = 0.5$, and (b) $t_1 = 1.5$ and $\gamma = 0.5$. Note the difference in the orbital character around $k = \pi$ for the two cases.

which leads to a single-particle dispersion given by $\epsilon(k) = -2t \cos(k) + 2i\gamma \sin(k)$. For the equilibrium Hermitian system ($\gamma = 0$), the ground state is given by $0 < k < \frac{\pi}{2}, \frac{3\pi}{2} < k < 2\pi$, which has an entanglement scaling $c = 1$ with low-energy states that disperse linearly, $H(k) \sim v_F |k| (c_k^{\dagger R} c_k^R + c_k^{\dagger L} c_k^L)$, where R, L specify the right- and left-moving modes.

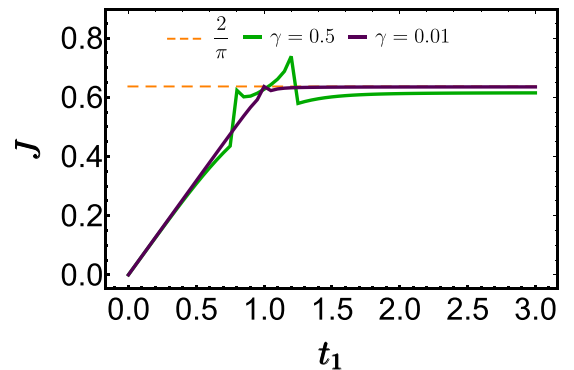


FIG. 12. Scaling of chiral current. Chiral current as a function of t_1 for different values of non-Hermitian coefficient γ . The current in the system saturates to $2/\pi$ as a function of t_1 for $t_1 \geq 1.0$. The current is dominated by the lowest of the two hopping scales t_1, t_2 .

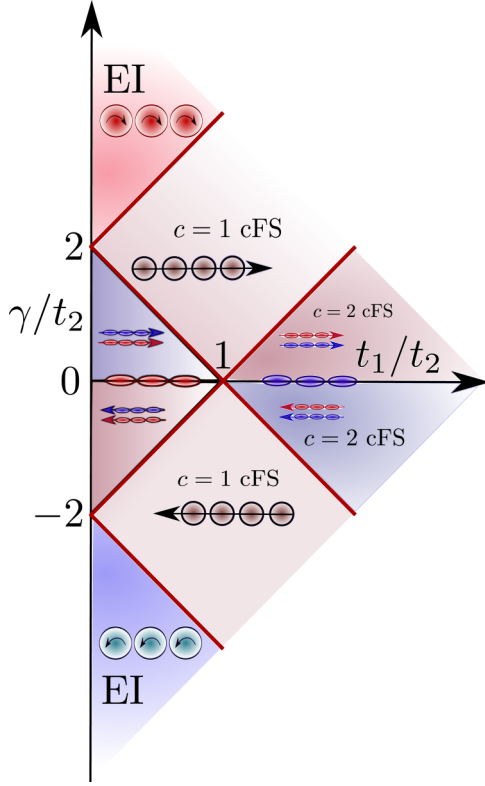


FIG. 13. Schematic of extended phase diagram. A schematic of the extended phase diagram of the system showing different nonequilibrium phases [see Eq. (2)] including the $c = 2$ cFS, $c = 1$ cFS, and the EI phase.

In the presence of any γ , the single-particle eigenvalues get a positive imaginary coefficient for $\pi < k < 2\pi$ leading to a steady state where $\pi < k < 2\pi$ are occupied.

The low-energy excitations are therefore *quadratically* dispersing fermions, albeit with a lifetime that is proportional to $\frac{1}{k}$,

$$H_{\text{HN}}(k) \sim [(-2 + k^2)t - i2\gamma k]c_k^{\dagger R}c_k^R + [(2 - k^2) - i2\gamma k]c_k^{\dagger L}c_k^L. \quad (29)$$

Along with excitations, another branch of short-lived excitations exist where the linearly dispersing fermions can scatter from the right- (left-) moving branch to the other left (right) branch with an energy $|(k - k_o)|$ ($k_o = \pi$), which are *linear* in momentum but with a finite lifetime (see Fig. 14). These excitations carry current in the opposite direction but eventually decay, thereby not changing the total steady-state current of the many-body state. Interestingly the subsystem scaling of the entanglement entropy continues to show $c = 1$. It is this feature that is characteristic of the chiral Fermi sea and is shared with the $c = 1$ chiral Fermi surface, which occurs in the complete phase diagram of Fig. 2 for the nH SSH model.

In a reduced Brillouin zone for a two-site unit cell, as is appropriate for our system, the above picture continues to hold, however with both the effective mass of fermions and

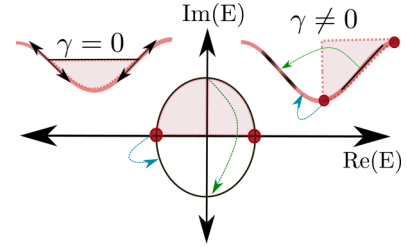


FIG. 14. Hatano-Nelson model at half-filling. In the absence of non-Hermiticity ($\gamma = 0$), the equilibrium system is given by two Fermi points with linearized excitations. In the presence of finite γ , the shifted Fermi sea has quadratic excitations at band minima and band edges (blue), and short-lived linear excitations (green).

lifetimes being γ - and t_1 -dependent,

$$H(k) \sim \left[\left(-\epsilon + \frac{k^2}{m} \right) + i\frac{k}{\tau} \right] c_k^{\dagger R} c_k^R + \left[\left(\epsilon - \frac{k^2}{m} \right) + i\frac{k}{\tau} \right] c_k^{\dagger L} c_k^L, \quad (30)$$

where $\epsilon = 2 + t_1 - \frac{\gamma^2}{16}$, $m^{-1} = (1/4) + \frac{t_1}{8} - \frac{\gamma^2}{128}$, and $\tau = \frac{8}{(2-t_1)\gamma}$ about $\gamma = 0, t_1 = 1$. Interestingly, the short-lived linear excitations now are also at small momentum given the zone-folding with a velocity scale given by $\sim t_1$ and a $\tau \propto \frac{1}{\gamma}$.

2. $c = 2$ cFS to $c = 1$ cFS

The $c = 2$ cFS is essentially two copies of the above Hatano-Nelson phase, however made out of bonding and antibonding orbitals of the dimerized system, which are at two different values of real energies. The natural point at which to investigate the $c = 2$ FS is to start from the $t_1 = 0, \gamma = 0$ point, where the Hamiltonian is exactly diagonalized by the following transformation:

$$c_{i\alpha} = \frac{1}{\sqrt{2}}(c_{i+1,A} + c_{iB}), \quad c_{i\beta} = \frac{1}{\sqrt{2}}(c_{i+1,A} - c_{iB}). \quad (31)$$

A perturbative γ when projected to just the α and β bands to leading order gives the following non-Hermitian Hamiltonian:

$$H_\alpha = \sum_i -(c_{\alpha i}^\dagger c_{\alpha i}) + \frac{\gamma}{4}(c_{\alpha i}^\dagger c_{\alpha, i+1} - \text{H.c.}), \quad (32)$$

$$H_\beta = \sum_i +(c_{\beta i}^\dagger c_{\beta i}) + \frac{\gamma}{4}(c_{\beta i}^\dagger c_{\beta, i+1} - \text{H.c.}), \quad (33)$$

where we have ignored the terms that mix α, β sectors. The above effective Hamiltonian essentially leads to *two* Galilean-boosted Fermi seas, which, however, are separated in real energies (see Fig. 6). A change of sign of γ leads to a different $c = 2$ cFS, where the currents are in the opposite direction. A similar interpretation is valid for large t_2 , where $t_1 \rightarrow 0$ and another set of dimers can be formed with *zero* polarization, $c_{i\alpha} = \frac{1}{\sqrt{2}}(c_{i,A} + c_{iB})$ and $c_{i\beta} = \frac{1}{\sqrt{2}}(c_{i,A} - c_{iB})$, with the effective non-Hermitian model given by Eq. (33) with a different orbital content. Again for $\gamma < 0$ the current direction changes. Therefore, one realizes four different kinds of $c = 2$ cFS (see Fig. 13) in the extended regime of γ and t_1 . Just like the discussion of the single Hatano-Nelson model in the last

subsection, here for each $c = 2$ cFS one obtains two copies of quadratic and linear excitation branches.

The transition from such a $c = 2$ cFS to a $c = 1$ cFS is essentially a Lifshitz transition characterized by exceptional point physics at $k = \pi$. The eigenvalues of the single-particle Hamiltonian at $k = \pi$ are given by [see Eq. (3)] $E_k = \pm\sqrt{(t_1 - t_2)^2 - \frac{\gamma^2}{4}}$, which shows that while the real spectrum is gapped as soon as $t_1 \neq t_2$ for $\gamma = 0$, there exists an extended regime for $\gamma > 2|(t_1 - t_2)|$ where the real eigenvalues are gapless, while the imaginary eigenvalues show a gap. Therefore, starting at any t_1, t_2 ($\gamma \rightarrow 0$) where a cFS-2 phase exists, $\Delta_{bg} \sim |t_2 - t_1|$ (see Fig. 6) with quadratically dispersing fermions. Upon tuning the non-Hermiticity parameter, γ , the branches merge at a critical value of $\lambda_c = 2|(t_1 - t_c)|$ close to which $\Delta_{bg} \sim \sqrt{\gamma_c - \gamma}$ —showing the characteristic nonanalyticity of a phase transition governed by exceptional point physics. Interestingly, both the real and imaginary eigenvalues of energy scale as $\sim\sqrt{k}$, reflecting the nonanalyticity of this low-energy theory at the exceptional points [69].

3. Entrapped insulator to $c = 2$ cFS

To understand the entrapped insulator, it is illustrative to discuss the large- γ limit, where a different band insulator can be obtained with eigenfunctions $\frac{1}{\sqrt{2}}(\pm \hat{c}_{iA}^\dagger + \hat{c}_{iB}^\dagger)$ —this has a finite *intra-unit-cell* current but no intercellular current. The transition from the $c = 2$ cFS ($t_1 < t_2, \gamma \rightarrow 0$) to an insulating steady state is again by an exceptional point, where the imaginary gap scales as $\sqrt{\gamma}$ near the phase transition.

V. TUNING BOUNDARY CONDITIONS

Having discussed the properties and phases of our system under periodic boundary conditions, we next study the system under open boundary conditions. For the Hermitian case, we know that an open system contains boundary modes that are robust to disorder. It is natural to question whether such modes can be obtained in a non-Hermitian system and how they affect the steady states.

More generally, we multiply a scaling factor, λ , to the boundary bond in order to smoothly tune between an open and a periodic problem (see [70]), and we discuss its effect on the steady-state physics. When $\lambda = 0$ (open boundary conditions), as has been reported in earlier studies focusing on the single-particle spectrum (see, for example, Ref. [32]), one finds four distinct regions as shown in Fig. 15. Briefly, for $\gamma > 2t_1$, all eigenvalues are real, while for $\gamma < 2t_1$ eigenvalues can have both real and imaginary components. Moreover, within the region $2\sqrt{t_1^2 - 1} < \gamma < 2\sqrt{t_1^2 + 1}$, one finds zero-energy eigenvalues that smoothly connect to topological boundary modes in the Hermitian limit ($\gamma = 0, t_1 < t_2$). Given that our steady states are constructed by populating modes with the largest imaginary component, such long-lived nonequilibrium states are only defined for $\gamma < 2t_1$, while for $\gamma > 2t_1$ one obtains a conventional equilibrium ground state which is obtained by minimizing the total real energy. This apparent mismatch between the thermodynamic phase diagram for the periodic and the open problem is, however, an artifact of extreme sensitivity of the nonequilibrium phases to the $\lambda = 0$ limit, and, as we show below, any infinitesimal λ leads to

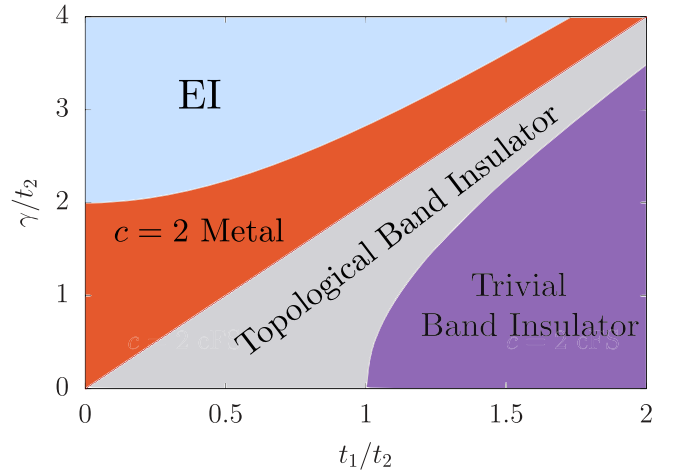


FIG. 15. Phase diagram under open boundary conditions. Four phases arise in the non-Hermitian SSH model [see Eq. (8)] under open boundary conditions. Of these (i) the entrapped insulator (EI) and (ii) $c = 2$ metal are nonequilibrium phases in their steady states, while (iii) the topological band insulator and (iv) the trivial band insulator are in equilibrium.

stable steady states, albeit with subtle effects arising due to topological boundary modes.

Four distinct phases can be identified in the open system as shown in Figs. 15 and 16. Out of these, (i) a trivial band insulator and (ii) a topological band insulator are the equilibrium phases that are smoothly connected to the Hermitian limit ($\gamma = 0$). While in the thermodynamic limit both of these regions have a bulk band gap, the latter has quasidegenerate boundary modes at zero real energies. The other two phases—(iii) $c = 2$ metal and (iv) an entrapped insulator—are nonequilibrium steady states that arise by populating the eigenmodes with the largest imaginary components. We find that the metallic phase has gapless excitations that can be long-lived, and it has a zero total current in the system (as is expected for an open system). Investigating the bipartite entanglement leads to a central charge $c = 2$ (see Fig. 17). Interestingly, this metallic phase contains two zero-energy modes which have both real and imaginary components that are zero. This leads to quasidegenerate steady states in the system, which can be excited via particle-hole excitations. Having discussed the many-body phases as realized in the completely open system, we now investigate their stability to weak hybridization (λ) between the boundary sites.

We find that, in the thermodynamic limit, any perturbatively small λ *immediately* leads to the nonequilibrium phases as realized in the periodic system as shown in Fig. 2. However, as λ is tuned, two phenomena generically occur: (a) boundary modes in regions of the metal and band insulator give way to Fermi seas, albeit with boundary modes either by changing the gap between the steady states or by leaky boundary modes, and (b) the steady-state current gets immediately saturated to the value in the periodic problem as soon as $\lambda \neq 0$. We therefore interpolate from the open (see Fig. 15) to the periodic system as a function of λ (see Fig. 2) to see how the steady state evolves. In the Hermitian limit ($\gamma = 0$) when $t_1 < t_2$, the

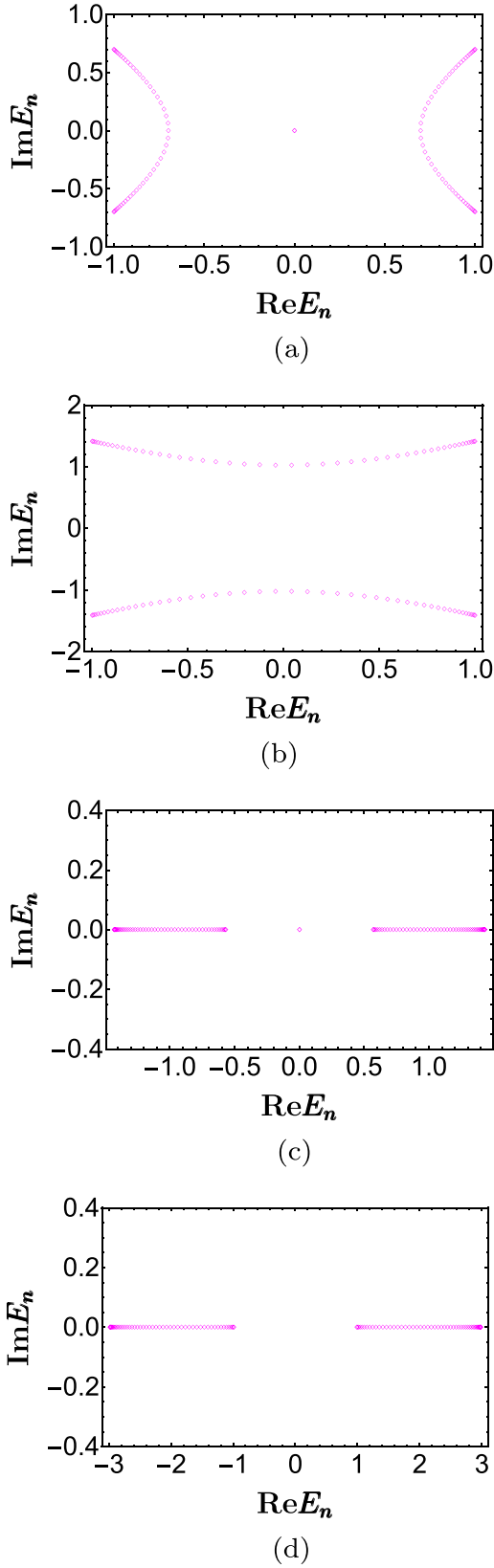


FIG. 16. Single-particle complex spectra under open boundary conditions. (a) $c = 2$ metal ($t_1 = 0.5$, $\gamma = 1.72$). (b) Entrapped insulator ($t_1 = 0.5$, $\gamma = 3.0$). (c) Topological band insulator ($t_1 = 0.5$, $\gamma = 0.5$). (d) Trivial insulator phase ($t_1 = 2.0$, $\gamma = 0.5$).

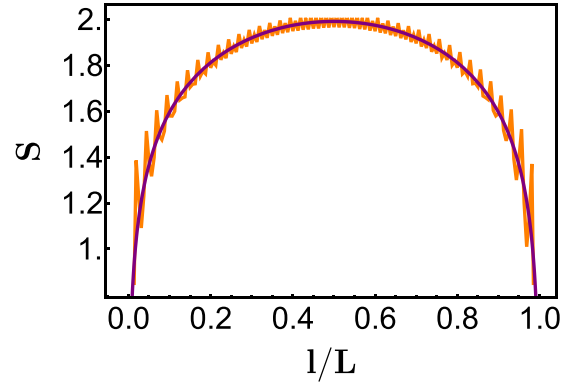


FIG. 17. Entanglement entropy for $c = 2$ metal. The entanglement entropy for $c = 2$ metal under open boundary conditions as a function of the bond length l/L for $L = 160$. The numerical data can be fit to $\frac{c}{6} \ln \left[\frac{L}{\pi} \sin \left(\frac{\pi l}{L} \right) \right]$, where $c/6 = 0.337$ (solid purple line). Here we have set $t_1 = 0.1$, $\gamma = 0.75$.

boundary modes for the open system hybridize and gap out (with the gap $\propto \lambda$), eventually merging with the bulk bands at $\lambda = 1$.

A. Instability to cFS-2 A

We start from the open system in either the topological or trivial band insulator, and we introduce a λ to interpolate to the $c = 2$ cFS. While the spectrum is purely real for $\lambda = 0$, any finite value of λ introduces an imaginary part to the eigenvalues and moves the boundary modes along the real line toward the two lobes [see the spectrum in Fig. 18(a)]. This immediately leads to a finite steady-state current as shown in Fig. 18(b) for a few representative values. Therefore, we find that the open boundary phase diagram is *not stable*, and immediately leads to a chiral metal phase. However, there is a distinction as to how the $c = 2$ cFS is approached either from topological or trivial band-insulator regimes. Note that the $c = 2$ cFS has six steady states with gaps given by Δ_{bg} and Δ_t (see Fig. 6). When λ is tuned such that the $c = 2$ CFS approaches a topological band insulator, two bulk modes move toward *zero* in the real spectrum thereby tuning both $\Delta_t \rightarrow \Delta_{bw}/2$ and $\Delta_{bg} \rightarrow 0$ [see Fig. 18(c)], thus offering a tunability between two many-body quasidegenerate steady states by occupying or emptying the boundary mode locally. It is in this sense that these steady states realized in $c = 2$ cFS-A are in fact *tunable* and are inherently distinct from the $c = 2$ cFS-B. Thus the role of single-particle boundary modes here is to provide an avenue for interesting quasidegenerate steady states that are boundary-tunable. Similar physics is at play when λ interpolates between $c = 2$ nonchiral metal realized in the open system to the $c = 2$ chiral FS. Again any finite value of λ immediately leads to a chiral current, and the existence of boundary modes, which, in turn, lead to quasidegenerate steady states (see Fig. 19).

B. Instability to $c = 1$ cFS

We next discuss the instability to another phase from the topological band insulator, where the system goes to the chiral

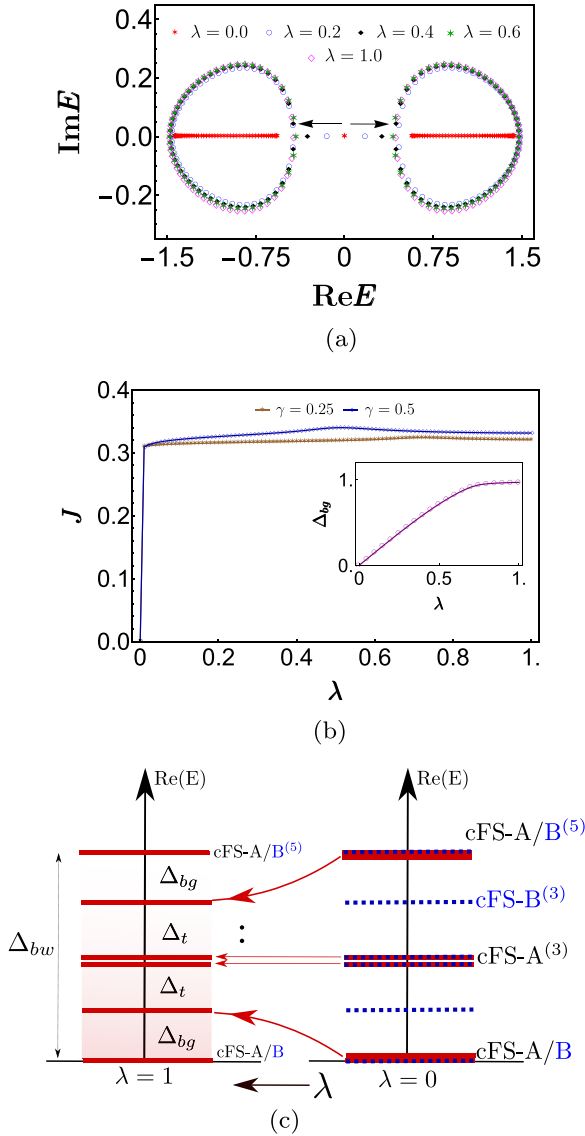


FIG. 18. Instability of the topological band insulator region to cFS-A. (a) The spectrum in the complex plane for different values of λ for $t_1 = 0.5$, $\gamma = 0.5$. (b) The current J as a function of λ . The inset shows the behavior of Δ_{bg} by tuning λ . (c) A schematic of the energy spectrum. Here $t_1 = 0.5$.

$c = 1$ FS. At $\lambda = 0$, given that we are starting at the topological band insulator, we have two zero-energy eigenmodes. However, unlike the instability to the $c = 2$ phase, here the boundary modes move along the imaginary axis leading to a finite lifetime for the boundary mode (see Fig. 20). The system immediately obtains a finite current and two degenerate steady states. Each of them, however, has an excitation over the boundary that has a finite lifetime. The way the value of the lifetime changes with λ is shown in the inset of Fig. 20(b). Unlike the previous case, the lifetime decreases exponentially with increasing λ , leading, therefore, to the *leaky* boundary modes.

The entrapped insulator phase in the open system gets smoothly connected to the periodic system and is therefore stable to the tunability of boundary conditions, as is expected

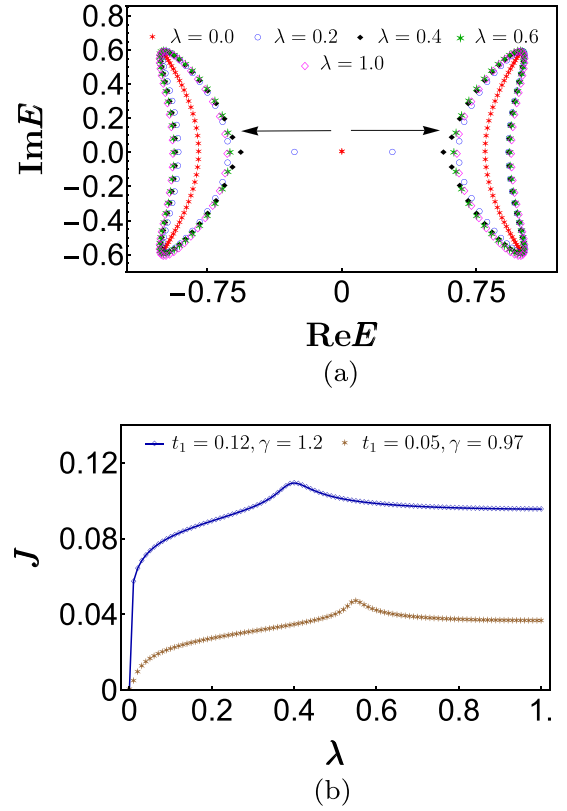


FIG. 19. Instability of the $c = 2$ metal region to $c = 2$ cFS-A. (a) The complex spectrum for different values of λ for $t_1 = 0.12$, $\gamma = 1.2$. (b) The current J variation with λ for two different representative values of t_1 and γ .

for a steady state with no finite current. In this regard, we have discussed the stability of all the phases we realized in the open system and the role of boundary modes in such steady-state physics.

VI. SUMMARY AND DISCUSSION

In this work, we revisited the nH-SSH model and the phases it realizes under finite filling. We found that the single-particle phase diagram gets reinterpreted in terms of distinct nonequilibrium phases of matter, which get realized at long times. We further analyzed each of the phases in terms of its correlations, gap to excitations, and entanglement features. Developing the low-energy theories of various phases and intervening transitions, we built a qualitative understanding of the phases and its excitations in terms of the spectral topology. We further tuned the boundary conditions to take the system from an open to a periodic problem, and we found that the nature of the equilibrium phases in the open system are perturbatively unstable to a weak coupling and leads to finite currents in the system.

An important question, which we have side-stepped here, is how such non-Hermitian Hamiltonians get realized in an experimental setting and where this is a valid effective description. While in open systems, where bath degrees of freedom are systematically integrated out and the effective density matrix of a system is evolved, one naturally uses the

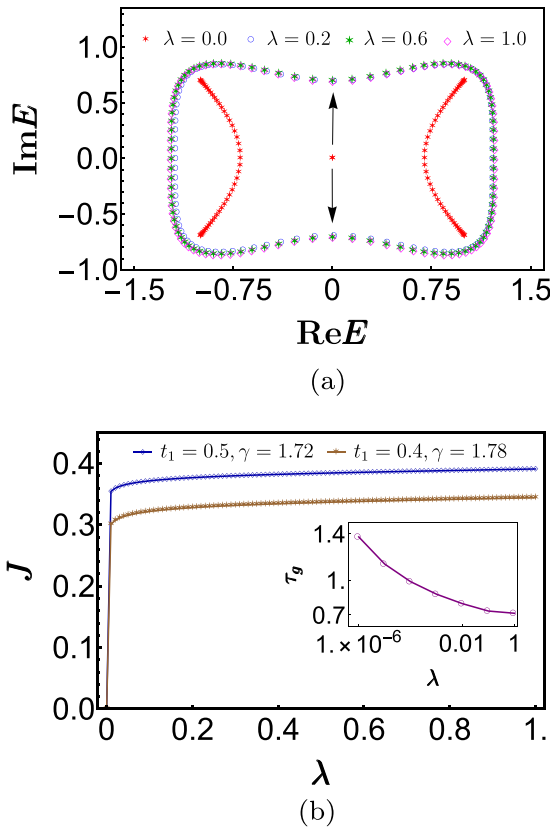


FIG. 20. Instability of the $c = 2$ metal region to $c = 1$ cFS. (a) Tuning of the complex spectrum with varying λ . (b) Variation of the current J with λ at two representative choices of t_1 and γ . (Inset: variation of the lifetime τ_g of the boundary excitations as a function of λ for $t_1 = 0.5, \gamma = 1.72$.)

Lindbladian approach, which can in general be non-Hermitian [9,71]. While in our system, we do not address how such a non-Hermitian Hamiltonian can be realized; concrete proposals addressing such questions have recently been suggested, for example in a quantum measurement setup [72]. Also see Ref. [73] for a realization in a Majorana chain setup. To realize the non-Hermitian phases we discuss here in such microscopic open systems, it will be crucial to study the competition between the timescales involved for realizing the

steady state itself and the occurrence of jump operators in the full Lindbladian [38,74]. Here we presume the existence of the nH-SSH system and that one can keep it at a finite density. This is a particularly useful construct where one may consider such non-Hermitian models and their steady states to be anomalous theories that get realized on the boundaries of higher-dimensional topological phases [58].

Our work opens up several avenues to explore. While here we discuss the long-time steady states, which are captured via an effective Fermi distribution in Eq. (15), it may be interesting to study how an equilibrium ground state evolves into such a steady state due to the introduction of any non-Hermiticity and if such dynamically evolving many-body states can be assigned to free Fermi distributions. One natural scope of expanding our findings is to consider higher dimensions, where one expects such chiral phases and entrapped insulating phases to be generic. An interesting direction will be to investigate the role of disorder and impurities in such systems, and the meaning of resulting topological protection in such many-body states obtained in the non-Hermitian phases. How an equilibrium state reaches such steady states in time and the corresponding dynamics of the density matrix due to introduction of non-Hermiticity is another interesting future scope. Similarly, the role of many-body physics and interactions is something that has been studied only recently [31,75–80] and is worth pursuing in the future. In conclusion, our different many-body perspective on the non-Hermitian phases can lead to interesting insights where the interplay of topology, entanglement, and correlations conspires to produce novel phases of quantum matter.

ACKNOWLEDGMENTS

A.B. is supported by the Prime Minister's Research Fellowship (PMRF). S.S.H. acknowledges MPI-PKS, Dresden for support during the project. A.A. acknowledges enlightening discussions with Animesh Panda, Sumilan Banerjee, Vatsal Dwivedi, Aabhaas Mallik, Abhisodh Prakash, and a related collaboration with Amit Chatterjee and Arghya Das. A.A. acknowledges partial financial support through the Max Planck partner group on strongly correlated systems at ICTS. A.A. acknowledges the visitor's program at MPI-PKS, Dresden for hospitality. A.N. is supported by the start-up grant (SG/MHRD-19-0001) of the Indian Institute of Science and by DST-SERB (Project No. SRG/2020/000153).

[1] X.-G. Wen, *Colloquium: Zoo of quantum-topological phases of matter*, *Rev. Mod. Phys.* **89**, 041004 (2017).
[2] A. W. W. Ludwig, Topological phases: classification of topological insulators and superconductors of non-interacting fermions, and beyond, *Phys. Scr.* **T168**, 014001 (2016).
[3] C.-K. Chiu, J. C. Y. Teo, A. P. Schnyder, and S. Ryu, Classification of topological quantum matter with symmetries, *Rev. Mod. Phys.* **88**, 035005 (2016).
[4] M. Z. Hasan and C. L. Kane, *Colloquium: Topological insulators*, *Rev. Mod. Phys.* **82**, 3045 (2010).

[5] X.-L. Qi and S.-C. Zhang, Topological insulators and superconductors, *Rev. Mod. Phys.* **83**, 1057 (2011).
[6] V. M. M. Alvarez, J. E. B. Vargas, M. Berdakin, and L. E. F. Foa Torres, Topological states of non-Hermitian systems, *Eur. Phys. J.: Spec. Top.* **227**, 1295 (2018).
[7] L. E. F. Foa Torres, Perspective on topological states of non-Hermitian lattices, *J. Phys.: Mater.* **3**, 014002 (2020).
[8] Y. Ashida, Z. Gong, and M. Ueda, Non-Hermitian physics, *Adv. Phys.* **69**, 249 (2020).

- [9] E. J. Bergholtz, J. C. Budich, and F. K. Kunst, Exceptional topology of non-Hermitian systems, *Rev. Mod. Phys.* **93**, 015005 (2021).
- [10] J. Carlström, Correlations in non-Hermitian systems and diagram techniques for the steady state, *Phys. Rev. Research* **2**, 013078 (2020).
- [11] J. Huber, P. Kirton, S. Rotter, and P. Rabl, Emergence of PT-symmetry breaking in open quantum systems, *SciPost Phys.* **9**, 052 (2020).
- [12] T. E. Lee, F. Reiter, and N. Moiseyev, Entanglement and Spin Squeezing in Non-Hermitian Phase Transitions, *Phys. Rev. Lett.* **113**, 250401 (2014).
- [13] T. E. Lee and C.-K. Chan, Heralded Magnetism in Non-Hermitian Atomic Systems, *Phys. Rev. X* **4**, 041001 (2014).
- [14] S. Lieu, M. McGinley, and N. R. Cooper, Tenfold Way for Quadratic Lindbladians, *Phys. Rev. Lett.* **124**, 040401 (2020).
- [15] B.-B. Wei and L. Jin, Universal critical behaviours in non-Hermitian phase transitions, *Sci. Rep.* **7**, 7165 (2017).
- [16] M. van Caspel, S. E. Tapias Arze, and I. Pérez Castillo, Dynamical signatures of topological order in the driven-dissipative Kitaev chain, *SciPost Phys.* **6**, 026 (2019).
- [17] F. Dangel, M. Wagner, H. Cartarius, J. Main, and G. Wunner, Topological invariants in dissipative extensions of the Su-Schrieffer-Heeger model, *Phys. Rev. A* **98**, 013628 (2018).
- [18] A. Panda and S. Banerjee, Entanglement in nonequilibrium steady states and many-body localization breakdown in a current-driven system, *Phys. Rev. B* **101**, 184201 (2020).
- [19] S. Lieu, Non-Hermitian Majorana modes protect degenerate steady states, *Phys. Rev. B* **100**, 085110 (2019).
- [20] A. Ghatak and T. Das, New topological invariants in non-hermitian systems, *J. Phys.: Condens. Matter* **31**, 263001 (2019).
- [21] Y.-B. Guo, Y.-C. Yu, R.-Z. Huang, L.-P. Yang, R.-Z. Chi, H.-J. Liao, and T. Xiang, Entanglement entropy of non-hermitian free fermions, *J. Phys.: Condens. Matter* **33**, 475502 (2021).
- [22] K. Wang, A. Dutt, K. Y. Yang, C. C. Wojcik, J. Vučković, and S. Fan, Generating arbitrary topological windings of a non-Hermitian band, *Science* **371**, 1240 (2021).
- [23] Z. Gong, Y. Ashida, K. Kawabata, K. Takasan, S. Higashikawa, and M. Ueda, Topological Phases of Non-Hermitian Systems, *Phys. Rev. X* **8**, 031079 (2018).
- [24] K. Kawabata, K. Shiozaki, M. Ueda, and M. Sato, Symmetry and Topology in Non-Hermitian Physics, *Phys. Rev. X* **9**, 041015 (2019).
- [25] C. H. Lee and R. Thomale, Anatomy of skin modes and topology in non-Hermitian systems, *Phys. Rev. B* **99**, 201103(R) (2019).
- [26] R. Resta, Macroscopic polarization in crystalline dielectrics: The geometric phase approach, *Rev. Mod. Phys.* **66**, 899 (1994).
- [27] H. Watanabe and M. Oshikawa, Inequivalent Berry Phases for the Bulk Polarization, *Phys. Rev. X* **8**, 021065 (2018).
- [28] D. J. Thouless, M. Kohmoto, M. P. Nightingale, and M. den Nijs, Quantized Hall Conductance in a Two-Dimensional Periodic Potential, *Phys. Rev. Lett.* **49**, 405 (1982).
- [29] M. Fruchart, R. Hanai, P. B. Littlewood, and V. Vitelli, Non-reciprocal phase transitions, *Nature (London)* **592**, 363 (2021).
- [30] S. Lieu, Topological symmetry classes for non-Hermitian models and connections to the bosonic Bogoliubov-de Gennes equation, *Phys. Rev. B* **98**, 115135 (2018).
- [31] E. Lee, H. Lee, and B.-J. Yang, Many-body approach to non-Hermitian physics in fermionic systems, *Phys. Rev. B* **101**, 121109(R) (2020).
- [32] L. Herviou, J. H. Bardarson, and N. Regnault, Defining a bulk-edge correspondence for non-Hermitian Hamiltonians via singular-value decomposition, *Phys. Rev. A* **99**, 052118 (2019).
- [33] S. Lieu, Topological phases in the non-Hermitian Su-Schrieffer-Heeger model, *Phys. Rev. B* **97**, 045106 (2018).
- [34] L. Jin and Z. Song, Bulk-boundary correspondence in a non-Hermitian system in one dimension with chiral inversion symmetry, *Phys. Rev. B* **99**, 081103(R) (2019).
- [35] S. Yao, F. Song, and Z. Wang, Non-Hermitian Chern Bands, *Phys. Rev. Lett.* **121**, 136802 (2018).
- [36] F. K. Kunst, E. Edvardsson, J. C. Budich, and E. J. Bergholtz, Biorthogonal Bulk-Boundary Correspondence in Non-Hermitian Systems, *Phys. Rev. Lett.* **121**, 026808 (2018).
- [37] J. S. Liu, Y. Z. Han, and C. S. Liu, Topological phases of a non-Hermitian coupled SSH ladder, *Chin. Phys. B* **28**, 100304 (2019).
- [38] F. Song, S. Yao, and Z. Wang, Non-Hermitian Skin Effect and Chiral Damping in Open Quantum Systems, *Phys. Rev. Lett.* **123**, 170401 (2019).
- [39] K. Esaki, M. Sato, K. Hasebe, and M. Kohmoto, Edge states and topological phases in non-Hermitian systems, *Phys. Rev. B* **84**, 205128 (2011).
- [40] H. Schomerus, Topologically protected midgap states in complex photonic lattices, *Opt. Lett.* **38**, 1912 (2013).
- [41] V. M. Martinez Alvarez, J. E. Barrios Vargas, and L. E. F. Foa Torres, Non-Hermitian robust edge states in one dimension: Anomalous localization and eigenspace condensation at exceptional points, *Phys. Rev. B* **97**, 121401(R) (2018).
- [42] C. Yin, H. Jiang, L. Li, R. Lü, and S. Chen, Geometrical meaning of winding number and its characterization of topological phases in one-dimensional chiral non-Hermitian systems, *Phys. Rev. A* **97**, 052115 (2018).
- [43] S. Yao and Z. Wang, Edge States and Topological Invariants of Non-Hermitian Systems, *Phys. Rev. Lett.* **121**, 086803 (2018).
- [44] P. St-Jean, V. Goblot, E. Galopin, A. Lemaître, T. Ozawa, L. Le Gratiet, I. Sagnes, J. Bloch, and A. Amo, Lasing in topological edge states of a one-dimensional lattice, *Nat. Photon.* **11**, 651 (2017).
- [45] S. M. Albrecht, A. P. Higginbotham, M. Madsen, F. Kuemmeth, T. S. Jespersen, J. Nygård, P. Krogstrup, and C. M. Marcus, Exponential protection of zero modes in Majorana islands, *Nature (London)* **531**, 206 (2016).
- [46] F. K. Kunst and V. Dwivedi, Non-Hermitian systems and topology: A transfer-matrix perspective, *Phys. Rev. B* **99**, 245116 (2019).
- [47] D. S. Borgnia, A. J. Kruchkov, and R.-J. Slager, Non-Hermitian Boundary Modes and Topology, *Phys. Rev. Lett.* **124**, 056802 (2020).
- [48] S. Masuda and M. Nakamura, Relationship between the electronic polarization and the generalized winding number in non-Hermitian systems, *J. Phys. Soc. Jpn.* **91**, 043701 (2022).
- [49] H.-G. Zirnstein, G. Refael, and B. Rosenow, Bulk-Boundary Correspondence for Non-Hermitian Hamiltonians via Green Functions, *Phys. Rev. Lett.* **126**, 216407 (2021).
- [50] V. M. Vyas and D. Roy, Topological aspects of periodically driven non-Hermitian Su-Schrieffer-Heeger model, *Phys. Rev. B* **103**, 075441 (2021).

- [51] Y. He and C.-C. Chien, Non-Hermitian generalizations of extended Su-Schrieffer-Heeger models, *J. Phys.: Condens. Matter* **33**, 085501 (2021).
- [52] N. Silberstein, J. Behrends, M. Goldstein, and R. Ilan, Berry connection induced anomalous wave-packet dynamics in non-Hermitian systems, *Phys. Rev. B* **102**, 245147 (2020).
- [53] T. Helbig, T. Hofmann, S. Imhof, M. Abdelghany, T. Kiessling, L. W. Molenkamp, C. H. Lee, A. Szameit, M. Greiter, and R. Thomale, Generalized bulk–boundary correspondence in non-Hermitian topoelectrical circuits, *Nat. Phys.* **16**, 747 (2020).
- [54] T. Hofmann, T. Helbig, F. Schindler, N. Salgo, M. Brzezińska, M. Greiter, T. Kiessling, D. Wolf, A. Vollhardt, A. Kabaši *et al.*, Reciprocal skin effect and its realization in a topoelectrical circuit, *Phys. Rev. Research* **2**, 023265 (2020).
- [55] S. Weidemann, M. Kremer, T. Helbig, T. Hofmann, A. Stegmaier, M. Greiter, R. Thomale, and A. Szameit, Topological funneling of light, *Science* **368**, 311 (2020).
- [56] H. B. Nielsen and M. Ninomiya, A no-go theorem for regularizing chiral fermions, *Phys. Lett. B* **105**, 219 (1981).
- [57] T. Bessho and M. Sato, Topological Duality in Floquet and Non-Hermitian Dynamical Anomalies: Extended Nielsen-Ninomiya Theorem and Chiral Magnetic Effect, *Phys. Rev. Lett.* **127**, 196404 (2021).
- [58] J. Y. Lee, J. Ahn, H. Zhou, and A. Vishwanath, Topological Correspondence between Hermitian and Non-Hermitian Systems: Anomalous Dynamics, *Phys. Rev. Lett.* **123**, 206404 (2019).
- [59] T. Yoshida and Y. Hatsugai, Correlation effects on non-Hermitian point-gap topology in zero dimension: Reduction of topological classification, *Phys. Rev. B* **104**, 075106 (2021).
- [60] F. H. M. Faisal and J. V. Moloney, Time-dependent theory of non-Hermitian Schrodinger equation: Application to multiphoton-induced ionisation decay of atoms, *J. Phys. B* **14**, 3603 (1981).
- [61] K. Zhang, Z. Yang, and C. Fang, Correspondence between Winding Numbers and Skin Modes in Non-Hermitian Systems, *Phys. Rev. Lett.* **125**, 126402 (2020).
- [62] I. Peschel, Calculation of reduced density matrices from correlation functions, *J. Phys. A* **36**, L205 (2003).
- [63] P. Calabrese and J. Cardy, Entanglement entropy and conformal field theory, *J. Phys. A* **42**, 504005 (2009).
- [64] P.-Y. Chang, J.-S. You, X. Wen, and S. Ryu, Entanglement spectrum and entropy in topological non-Hermitian systems and nonunitary conformal field theory, *Phys. Rev. Research* **2**, 033069 (2020).
- [65] B. Derrida, Non-equilibrium steady states: fluctuations and large deviations of the density and of the current, *J. Stat. Mech.* (2007) P07023.
- [66] N. Hatano and D. R. Nelson, Localization Transitions in Non-Hermitian Quantum Mechanics, *Phys. Rev. Lett.* **77**, 570 (1996).
- [67] J. K. Asbóth, L. Oroszlány, and A. Pályi, A short course on topological insulators, *Lect. Notes Phys.* **919**, 166 (2016).
- [68] R. Resta and D. Vanderbilt, Theory of polarization: a modern approach, in *Physics of Ferroelectrics* (Springer, Berlin, Heidelberg, 2007), pp. 31–68.
- [69] C. Aron and C. Chamon, Landau theory for non-equilibrium steady states, *SciPost Phys.* **8**, 074 (2020).
- [70] R. Koch and J. C. Budich, Bulk-boundary correspondence in non-Hermitian systems: Stability analysis for generalized boundary conditions, *Eur. Phys. J. D* **74**, 70 (2020).
- [71] A. Altland, M. Fleischhauer, and S. Diehl, Symmetry Classes of Open Fermionic Quantum Matter, *Phys. Rev. X* **11**, 021037 (2021).
- [72] C. Fleckenstein, A. Zorzato, D. Varjas, E. J. Bergholtz, J. H. Bardarson, and A. Tiwari, Non-Hermitian topology in monitored quantum circuits, *arXiv:2201.05341*.
- [73] S. Diehl, E. Rico, M. A. Baranov, and P. Zoller, Topology by dissipation in atomic quantum wires, *Nat. Phys.* **7**, 971 (2011).
- [74] Z. Zhou and Z. Yu, Skin effect in quadratic Lindbladian systems: an adjoint fermion approach, *arXiv:2110.09874*.
- [75] F. Alsallom, L. Herviou, O. V. Yazyev, and M. Brzezińska, Fate of the non-Hermitian skin effect in many-body fermionic systems, *arXiv:2110.13164*.
- [76] T. Liu, J. J. He, T. Yoshida, Z.-L. Xiang, and F. Nori, Non-Hermitian topological Mott insulators in one-dimensional fermionic superlattices, *Phys. Rev. B* **102**, 235151 (2020).
- [77] S. Mu, C. H. Lee, L. Li, and J. Gong, Emergent fermi surface in a many-body non-Hermitian fermionic chain, *Phys. Rev. B* **102**, 081115(R) (2020).
- [78] R. Shen and C. H. Lee, Non-Hermitian skin clusters from strong interactions, *arXiv:2107.03414*.
- [79] W. Zhang, F. Di, H. Yuan, H. Wang, X. Zheng, L. He1, H. Sun, and X. Zhang, Observation of non-Hermitian many-body skin effects in Hilbert space, *arXiv:2109.08334*.
- [80] T. Yoshida, Real-space dynamical mean field theory study of non-Hermitian skin effect for correlated systems: Analysis based on pseudospectrum, *Phys. Rev. B* **103**, 125145 (2021).